LAPPEENRANTA UNIVERSITY OF TECHNOLOGY

Faculty of Technology

LUT Energy

Master's Degree Programme in Energy Technology

Antton Tapani

DEVELOPMENT OF SOLAR CENTRAL RECEIVER SYSTEM MODEL FOR DYNAMIC PROCESS SIMULATION

Examiners: Professor, D.Sc. (Tech.) Timo Hyppänen

   Associate Professor, D.Sc. (Tech.) Tero Tynjälä

Supervisor: Senior Scientist, M.Sc. (Tech.) Matti Tähtinen

   Research Scientist, M.Sc. (Tech.) Elina Hakkarainen

   VTT Technical Research Centre of Finland

ABSTRACT

Antton Tapani

Development of solar central receiver system model for dynamic process simulation

Concentrated solar power (CSP) is an effective way of producing clean renewable energy, and the interest in utility scale installations is growing. However, the variable nature of solar energy makes predicting power plant performance challenging, which also makes new investments in the field risky. Full plant behaviour and project profitability can most effectively be understood through carefully conducted dynamic simulation off the entire facility.

The objective of this master's thesis is to develop an efficient computational model for solar central receiver systems, including heliostat field and the receiver system. The model is to be used in conjunction with the dynamic process simulation program Apros, owned and developed by VTT and Fortum. The presented model is composed of several individual component models, which can be considered separately from each other. A fast discrete ray tracing approximation is used to model the heliostat field's optical behaviour. This model uses approximation to reduce computing time while maintaining good accuracy. Atmospheric effects and receiver losses are accounted for by correlation models found in literature. The models are implemented as Apros components for convenient use within process simulations.

All individual parts of the model are shown to be working correctly and accurately, and the model performs well under Apros simulations. Although full system validation has not been performed, the model is considered accurate and usable.

TIIVISTELMÄ

Keskittävä aurinkovoima (CSP) on tehokas tapa tuottaa puhdasta uusiutuvaa energiaa, ja kiinnostus uusien laitosten rakentamiselle on kasvussa. Aurinkovoiman muuttuva luonne kuitenkin tekee voimalaitosten suorituskyvyn ennakoimisen haastavaksi, mikä tekee kaupalliset investoinnit riskialtteiksi. Koko laitoksen dynaaminen simulointi on paras tapa tarkastella laitosten käyttäytymistä ja kannattavuutta.

Tämän diplomityön tavoitteena on kehittää tehokas laskennallinen malli keskeisvastaanottimelle ja peilikentälle. Mallia käytetään yhdessä Apros voimalaitossimulointiohjelmiston kanssa. Apros-ohjelmistoa kehittävät VTT ja Fortum. Esitetty malli koostuu useasta itsenäisestä osamallista, joita voidaan käsitellä erillään toisistaan. Peilikentän optiikan mallinnukseen käytetään diskreettiä ray trace approksimaatiota. Tämä malli vähentää laskenta-aikaa likimääräistyksillä heikentämättä laskentatarkkuutta merkittävästi. Ilmakehän vaimentavia vaikutuksia ja vastaanottimen lämpöhäviöitä mallinnetaan kirjallisuudesta lainatuilla korrelaatiomalleilla. Mallit on toteutettu Apros-komponentteina, joiden käyttö simulaatioissa on vaivatonta.

Kaikkien osamallien todetaan toimivan oikein ja tarkasti, ja malli toimii tehokkaasti Apros simulaatioiden yhteydessä. Mallin täydellistä yhtenäistä validointia ei ole toteutettu, mutta mallia voidaan silti pitää tarkkana ja käyttökelpoisena.

PREFACE

One rarely gets an opportunity to work on a project that so perfectly combines one's personal activities and academic education. Such was the opportunity to participate in foundational solar power modelling development efforts at the heart of Finnish technology research, VTT Technical Research Center of Finland. It has been very pleasant to discover that there exists a lot of overlap between the fields of 3D-graphics and solar concentrator modelling. This thesis was commissioned by VTT under the project "Combination of Concentrated Solar Power with Circulating Fluidized Bed Power Plants" financed by Tekes – the Finnish Funding Agency for Innovation.

I was given considerable freedoms in both the design and implementation details of the developed central receiver model, which kept the project engaging and fascinating throughout the development time. While it is often easy to lose sight of the bigger picture whilst working on such a large project, the feedback I got from my supervisors Matti Tähtinen and Elina Hakkarainen kept me well on track with development goals. Likewise comments from the examiners Timo Hyppänen and Tero Tynjälä were immensely valuable for keeping the thesis well-structured and understandable for general audience. I heartily thank everyone involved.

Jyväskylä, 15.5.2016
Antton Tapani

TABLE OF CONTENTS

APPENDICES

NOMENCLATURE

A	area	m^2
FC	convection factor	-
h	specific enthalpy	kJ/kg
I	irradiance	W/m^2
$\dot{m}$	mass flow	kg/s
OR	opening ratio	-
R	slant range	km
V	wind velocity	m/s
Z	solar zenith angle	rad

Greek symbols

α	absorptivity, elevation angle	-, rad
β	scattering coefficient	-
σ	standard deviation	-
ε	emissivity	-
ξ	broadband extinction coefficient	-
θ	angle	rad

Subscripts

a	ambient
ap	aperture
atm	atmospheric
col	collector
cos	cosine
eff	effective
hs	heliostat
loc	local
maj	major
mc	Monte Carlo
min	minor
ray	ray
rec	receiver
s	site elevation
sun	sun
T	tower
tot	total
w	water
z	zenith

ABBREVIATIONS

APROS	The Advanced Process Simulation Environment
CFD	Computational Fluid Dynamics
CSP	Concentrated Solar Power
CRS	Central Receiver System
DNI	Direct Normal Irradiance
ESRA	European Solar Radiation Atlas
GIS	Geographical Information System
GUI	Graphical User Interface
HTF	Heat Transfer Fluid
JSON	JavaScript Object Notation
LFR	Linear Fresnel Reflector
PTC	Parabolic Trough Collector
STE	Solar Thermal Electricity

GLOSSARY

Aberration

Effect occurring in curved reflectors, where light does not correctly converge into a perfect focal point.

Abstraction

Level of detail that is being considered at any given context.

Apros

A dynamic process simulation software developed by VTT and Fortum

Blender

Graphical 3D modelling tool. Free open source software.

Canting

Curvature added to flat panel mirrors by dividing them to facets that are individually angled to better direct radiation toward the receiver center

Collector

The collection of mirrors that redirect radiation toward the **receiver**

Often used interchangeably with **heliostat field** in the thesis.

Collimated light

Light in which all rays travel in the same direction.

Dynamic link library (dll)

A compiled binary file containing program instructions. Other programs can import this file and make calls to the functions in it. Also known as shared object (so) under Unix-like systems.

Geometry

Used as shorthand referring to the layout, shape and dimensions of heliostats.

Instance (computing)

Identical copy with shared implementation, but different internal state. Multiple instances of the same object or model can operate at the same time without affecting each other.

Json (computing)

JavaScript Object Notation. Commonly used general purpose data serialization and storage format. Can be used across multiple programming languages.

Linke turbidity coefficient

Number of clean and dry optical atmospheres that would produce the same radiation attenuation as the real atmosphere.

Layout

The arrangement of heliostat locations in the field.

Monte Carlo algorithm

A family of probabilistic computation algorithms based on approximating a solution by analysing randomly generated data items. Does not refer to any specific algorithm, but any algorithm with similar characteristics.

Native (computing)

Existing and well supported. Part of a system or environment.

Precipitable water content (w)

The amount of water contained in vertical atmospheric column with unit area cross section. Measured in cm of liquid, when all the water in the column is condensed to liquid.

Primitive (computing)

Foundational component. A primitive cannot be divided into constituent parts within the same level of abstraction.

Receiver

Structure to gather radiation on a surface and conduct heat to heat transfer fluid.

Spill loss

Portion of reflected light that falls outside the receiver.

1. INTRODUCTION

Demand for efficiently produced carbon free heat and electricity has steadily grown among the population worldwide, and it has been a key topic in global political arena over the past few decades. While the demand is present, and artificial incentives and mandates have aided adoption of premature technologies, they still have to prevail in highly cost competitive marketplaces already saturated with more reliable fossil fuels and nuclear power. High capital costs and uncertain markets make it difficult for new companies to enter the competition.

Solar power faces technical and economic challenges that are largely not present in the prevailing energy industry. High confidence in the power plant's performance is vital for securing construction loans, as the loan giver must have reliable guarantees for the return of the investment. Fossil fuel based technologies are technically mature and proven to be reliable investments, so financial contracts are easy to secure. This is not necessarily the case with solar technologies.

Accurate and robust simulation of full solar power plant processes is the most reliable method for proving long term profitability of a power plant design. However, the diffuse and unpredictable nature of solar power makes building accurate models very challenging. Sudden changes in solar irradiation can introduce instabilities into the process and cause loss of power or reduced efficiency even if the plant has thermal storage or fossil fuel based backing. Full behavior of the system has to be understood in advance. This can be most effectively achieved through carefully conducted dynamic simulation of the entire system.

Although most of the current solar thermal capacity consists of parabolic trough collectors (PTC), there is still interest for central receiver systems (CRS) as they can potentially offer higher efficiencies and better thermal storage capabilities than other forms of solar thermal power.

1.1 Background

The interest in renewable power can be conveniently quantified by examining the rates of investments in the industry over the past few years. Figure 1.1 shows the distribution of investments in new power production capacity each year from 2002 to 2014 for each production type.
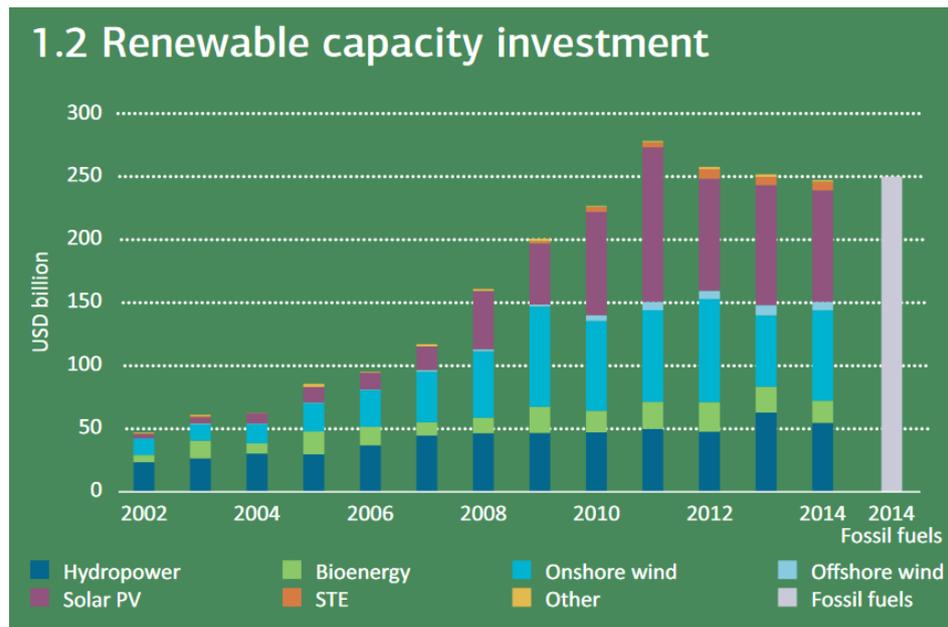

Figure 1.1: Global renewable capacity investment by year and type (IEA, 2015, 21)

In Figure 1.1 STE refers to solar thermal electricity, and covers all forms of concentrated solar power (CSP) whose primary purpose is to generate electricity for the grid. Solar PV refers to photovoltaic solar panels, and it can be seen that investments in the past have been focused on this type of solar power. This can likely be explained by the ease of installation in both large and small scale, and the ease of operation of photovoltaic systems. However, the significant advantage concentrated solar power has over photovoltaic solar panels is the ability to use large scale thermal energy storage. While electrochemical storage media exist for use with direct electricity generation, their grid scale utilization is not economically viable or technically feasible.

While comparatively small, the investments in STE have been approximately 1.8 billion USD annually since 2009 (IEA, 2014). Majority of this is in the form of

parabolic trough power plants (Figure 1.2), which is the most mature of the solar collector technologies. These plants use an elongated parabolic mirror to focus light on a pipe surface, where heat transfer fluid (HTF) is heated to a high temperature. The fluid is circulated through the system to a power conversion process to generate electricity. The mirror assembly is most often installed in north-south direction and follows the sun's apparent movement across the sky by rotating around one axis. The whole installation including the focal point rotates with the armature. More details on the physics behind a solar concentrator are covered in chapter 2.

Figure 1.2: Parabolic trough collector (Richter et al., 2013, 134)

Linear Fresnel concentrator (Figure 1.3) operates much the same way as parabolic troughs. Light is reflected from the concentrator along a pipe surface, but instead of the whole installation moving, smaller linear sections swivel on one axis in such a way that sunlight is always reflected on the receiver pipe surface. Fresnel collectors are more compact and can potentially reach somewhat higher temperatures than parabolic troughs.

Figure 1.3: Linear Fresnel reflector (Altanova-Energy).

Optical performance of a linear collector can be confirmed experimentally with relatively simple machinery consisting of a short segment of the mirror installation mounted on a rotating platform as seen in Figure 1.4. This helps in creating experimentally based models of full size power plants to accurately assess their performance before construction, which in part can explain the popularity of linear concentrators.

Figure 1.4: Linear concentrator test platform (Sandia National Laboratories)

Similar technique is not possible for modelling central receiver systems as the heliostat field is irregular in shape and evaluating small field segments will not give accurate description of the overall field performance. Small changes in field layout and mirror dimensions can have a large impact on immediate power output as well as

time variant behavior of the power plant as a whole. An accurate full system model is therefore required to accurately assess the power plant performance before construction. This serves as the main motivation behind this thesis.

1.2 Research objectives, questions and delimitations

The development effort associated with this thesis was initiated with the decided goal of augmenting the process simulation program Apros with fast and accurate modeling features regarding solar towers and heliostat fields. As the solar energy industry grows worldwide, developing modelling capabilities for such technologies becomes increasingly important.

The model is to be used in high performance process simulations within the Apros software. Complete Apros simulations of power plants can consist of thousands of individual components, each of which has associated processing requirements. These process models must also be able to run simulations tens or hundreds of times faster than real time. The model described in this thesis will act as one of these process components, and the processing power requirements must be as low as possible to avoid straining rest of the Apros process model unnecessarily.

There were no strict requirements for the methods to be used in the final modelling toolset, as long as the required tools are readily available for VTT, the model is widely applicable and the results are accurate. All details of the modelling research and implementation were left for the author to consider.

At the preliminary stages of the thesis work, it was considered an option to use existing CSP modeling tools to produce case specific regression models. However, this was deemed too restrictive even in ideal cases, and this approach was given up in favor of more general model development. The development effort was instead focused on complete implementation of the full model rather than its practical uses. This level of development requires considerable amount of research for all the model components and their efficient implementations, but has the advantage of being fully modifiable and adaptable, if future cases require further development.

Solar power is highly dependent on local conditions of each plant location. Therefore the model must be able to account for large number of parameters. Furthermore, solar tower systems depend on the configuration and layout of the associated heliostat field, making each power plant unique and model generalization challenging.

The final requirement of the thesis work is to implement the models as Apros process components and present a simple functional Apros process simulation that includes the solar collector and receiver models as process components. Also in this case the design choices were left to the author with the directive that the components must be easily configurable and connect logically to any process simulation.

Optimization of the heliostat field layout is a closely related to the topics of the thesis, however this is only tangentially considered in the model implementation and is not considered part of the thesis work. The presented models and their implementation are still efficient enough for optimization tasks, given suitable heuristics. One suitable methodology for this is described in (Noone et al. 2012).

1.3 Research methodology

Theoretical research was done primarily based on scientific articles and textbooks in the field of concentrated solar power and mathematics. Additional miscellaneous on-line resources for mathematical algorithms and implementation details were utilized where needed. Research on computational algorithms was additionally done by experimentation and benchmarks to find the most efficient implementations of the most numerically intensive algorithms.

1.4 Structure of the thesis

The thesis consists of several distinct parts
- Background information and motivation behind the thesis (Chapter 1)
- Theoretical description of the problem domain in general (Chapter 2)
- A review of existing modelling tools (Chapter 3)
- Model implementation details (Chapter 4)
- Practical use of the model (Chapter 5)

Theoretical part (Chapter 2) contains description of basic physical principles of central receiver systems as well as examples of technologies that the development effort aims to cover. This chapter outlines the physical properties that need to be considered during model development as well as some engineering details. The description is given at a very general level within this chapter, and each presented topic is examined in more detail together with model implementation details in chapter 4. Model validation is presented in chapter 4.5 where computations performed by each part of the model are compared to reference data.

Practical use of the model with Apros simulations is presented in chapter 5. Brief description of general usage of Apros itself is presented, followed by example model involving a heliostat field, solar receiver and a section of the steam loop within a solar power plant.

2. SOLAR CENTRAL RECEIVER TECHNOLOGY

While there are number of different types of solar collectors, this thesis only considers the modeling of central receiver systems, and therefore only covers the governing principles for this facility type. Chapter 2.1 explains general physical principles that govern the operation of central receiver system. Chapter 2.2 contains examples of existing solar collector and receiver technologies.

2.1 Basic principles

For illustration, this chapter treats solar radiation as consisting of individual rays whose path can be traced as straight lines. For the purposes of CSP design and modelling, the most fundamental interaction of light with the environment is total reflection seen in Figure 2.1.
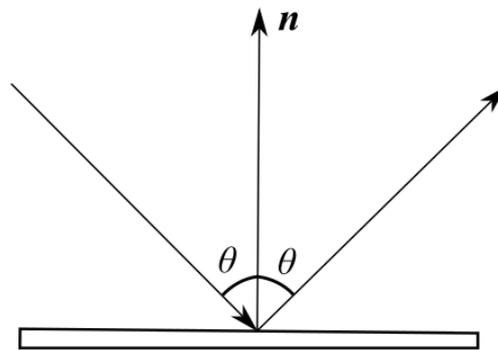
Figure 2.1: Reflection of light from a mirror. Incoming angle is equal to the outgoing angle.

All solar concentrator technologies are based on the same basic principle. Radiation from the sun arriving to an area is directed and concentrated to a receiving surface, which heats up to a high temperature. In all cases the concentration is done by sun tracking mirrors, whose arrangement depends on the type of concentrator used as outlined in chapter 1. In central receiver systems the sun tracking is done with mirror panels mounted on armatures that turn on two axes as seen in Figure 2.2.
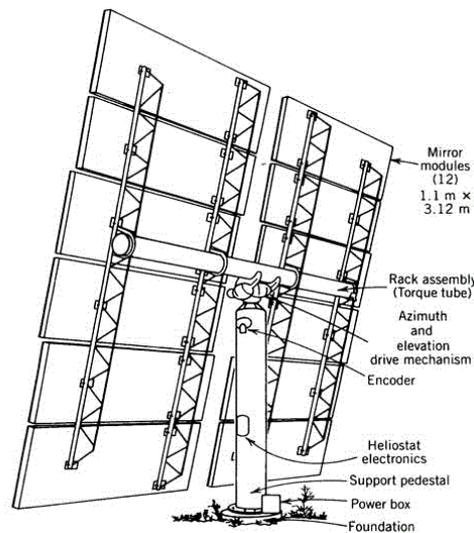
Figure 2.2: Single heliostat assembly (Southern California Edison)

On the receiver, heat is conducted to a heat transfer fluid, which is usually water, molten salt or oil. In case of water, high pressure steam is produced and it is used to directly drive turbines to produce electricity. Illustration of the general principles of central receiver solar plant with steam loop is shown in Figure 2.3. When molten salt or oil is used as the heat transfer medium, a heat exchanger is also required to transfer heat into a steam loop, wherein electricity is generated with a conventional steam turbine. Other heat transfer mediums such as air or solid particles can be used as well, but their uses are currently limited to smaller scale research facilities and are not prevalent in the industry.
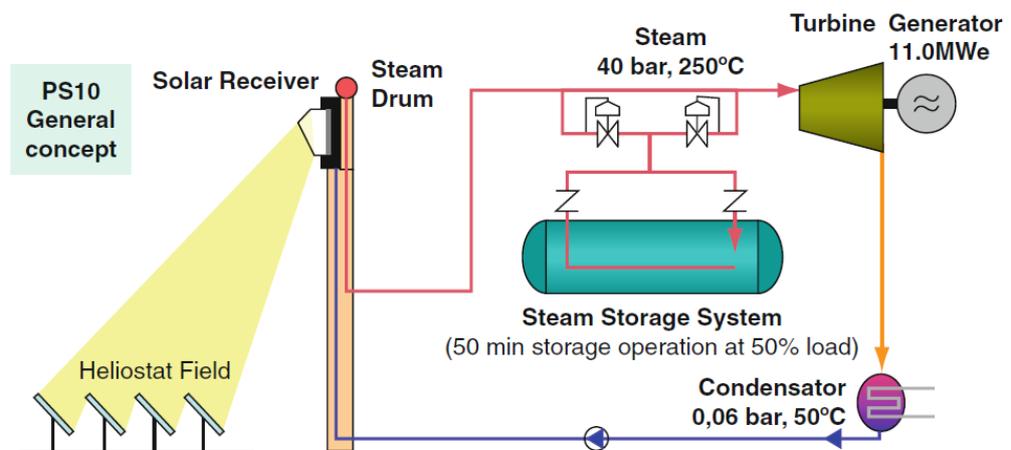

Figure 2.3: Conceptual power plant process of the PS10 solar plant. (Richter et al., 2013, 48)

One intriguing prospect of central receiver systems is the ability to use high temperature thermal energy storage. While other types of solar collectors can use thermal storage, central receiver plant can achieve higher efficiencies and storage capacities due to higher receiver temperatures. When molten salt is used as heat transfer medium, the hot salt from the receiver can be circulated through a hot storage tank when solar radiation is in excess to the needs of the grid. Conversely, when the sun does not shine, hot salt is circulated from the hot storage tank through the steam generator. Illustration of a central receiver plant with salt based heat transfer loop, salt storage and separate steam generator is shown in Figure 2.4.
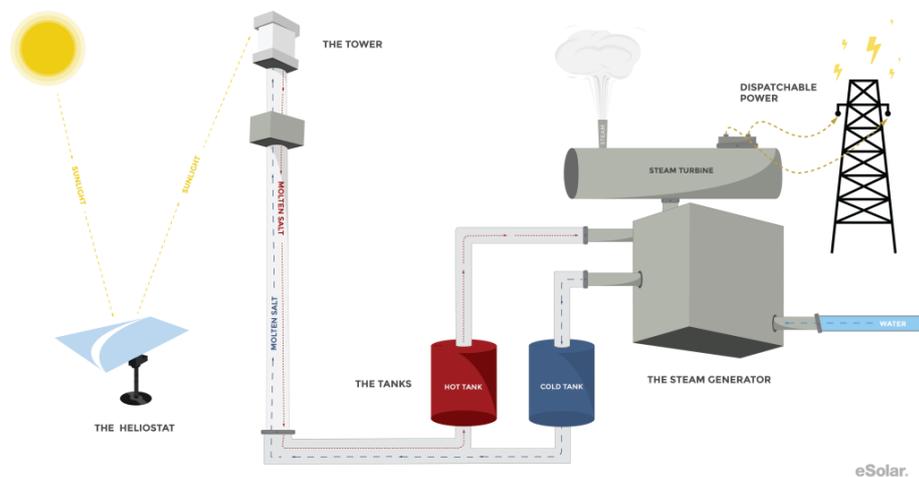

Figure 2.4: Central receiver power plant with molten salt storage (eSolar)

Figure 2.5 shows an example case, where electricity production is shifted from peak solar output toward a peak evening usage period by using stored heat.
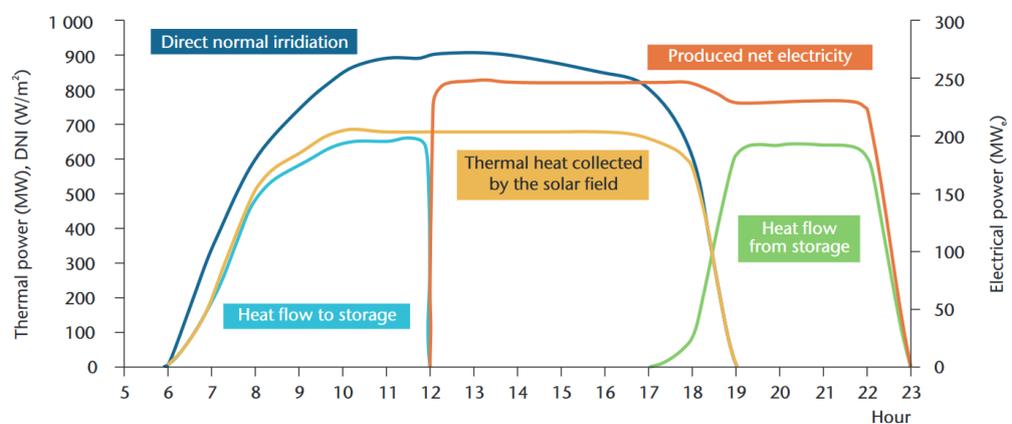

Figure 2.5: Thermal energy storage dispatching over time. (IEA,2014,14)

The sun, as it appears in the sky, is not a point source of light, but has an apparent disc shape. Because of this disc shaped source, the beam of direct light is not perfectly collimated, but has slight spread as some of the radiation originates from the edge of the disc and arrives at an angle. Figure 2.6 shows simplified example, in which rays of light are traced from the disc source through two points on a reflector illustrating the spreading of the light beam. This spread is further amplified by light scattering happening in the Earth's atmosphere.
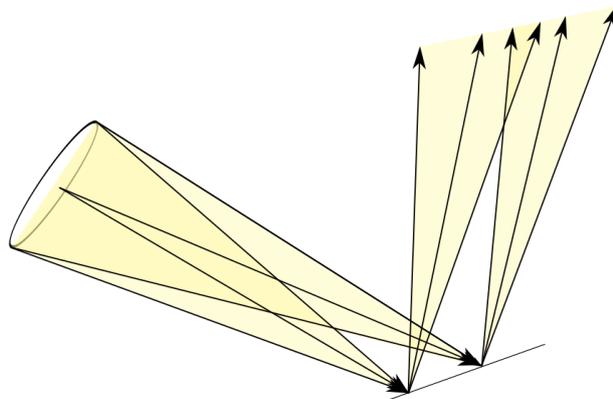
Figure 2.6: Solar rays passing through two points on a reflector. Spreading of the light is exaggerated for clarity.

In addition to sun shape, number of surface factors affect the reflected ray's direction. These are outlined in equation (1). Each of the factors can be considered to be roughly normally distributed, so they can be represented with individual standard deviations.

$$\sigma_{\text{slope,effective}}^2 \approx \sigma_{\text{specularity}}^2 + \sigma_{\text{slope}}^2 + \sigma_{\text{shape}}^2 + \sigma_{\text{tracking}}^2 \qquad (1)$$

Shape and slope errors both describe the macroscopic variation of mirror surfaces. In most practical cases mirrors are sufficiently large to allow representing both errors with a single value. Tracking errors occur when the mirrors are not aligned correctly due to imperfect drive mechanism, poor calibration, wind or number of other small factors. Specularity error is caused by microscopic surface defects that will scatter light even in otherwise perfectly constructed mirrors. From the point of view of reflected rays, all these errors together appear to have a statistically consistent

scattering effect, which can be represented by a single error variable $\sigma^2_{\text{slope,effective}}$. Deviation of the reflected ray from ideal reflection path is illustrated in Figure 2.7. (Lee, 2014, 300)
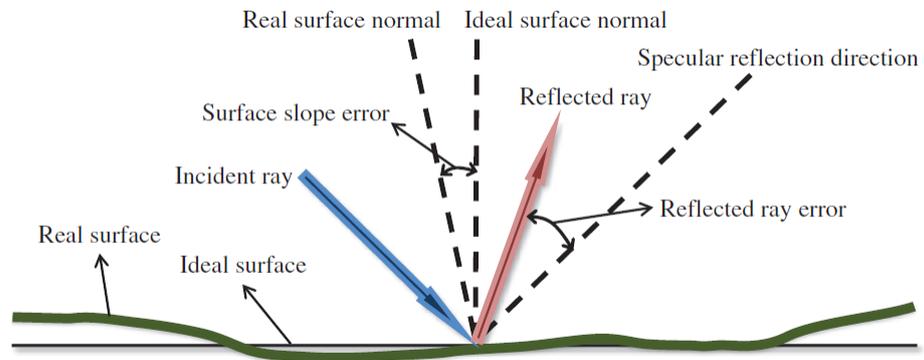
Figure 2.7: Reflected ray error. Reflected ray deviates from ideal reflection direction due to surface defects. (Lee,2014,300)

Together with the sun shape, the surface slope error cause the reflected beam of light to spread. Focusing the light perfectly becomes impossible and some of it inevitably misses the receiver. This is known as **spill loss**. Illustration of spill loss is seen in Figure 2.8.
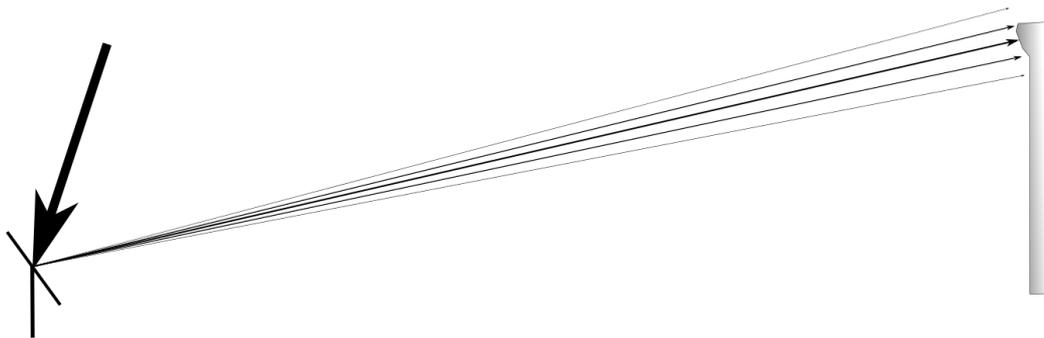
Figure 2.8: Spill loss. Due to surface imperfections and environmental factors, the reflected beam of light spreads and some of the radiation misses the receiver.

The solar irradiance entering the earth's atmosphere is $E_0 = 1367 \frac{\text{W}}{\text{m}^2}$ (Duffie & Beckman, 2013, Part 1, 6). This is also known as the solar constant. Portion of this

light gets absorbed and scattered by the earth's atmosphere, before it reaches the collector. The attenuated light intensity that reaches the ground level is often referred to as direct normal irradiance (DNI) or direct beam irradiance. DNI is measured as radiation intensity against a plane that is perpendicular to the path of the unscattered light. Large number of models for estimating DNI exist in literature (Badescu et al., 2012), and care should be taken when selecting a model to ensure its applicability to any given case.

In addition to global attenuation, local light attenuation in the lowest atmospheric layer has a significant impact on the final radiation intensity. This attenuation is caused by absorption by air molecules and water vapor as well as scattering caused by aerosols. The scattered light is not absorbed in the atmosphere, but its path is diverted and it does not contribute to the irradiance at the receiver. This is illustrated in Figure 2.9
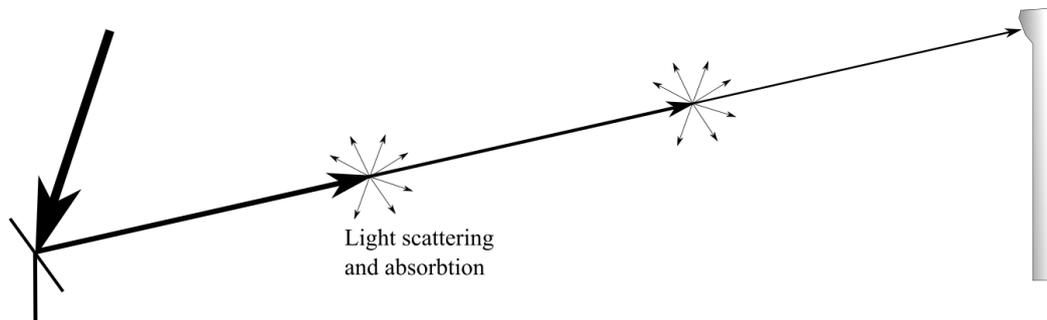
Figure 2.9: Local light attenuation between mirrors and the receiver due to scattering and absorption.

For flat panel heliostats, the spot cast on the receiver is comparable to the size of the mirror. This becomes a problem with larger mirrors as the radiation is distributed on wider area making the receiver unreasonably large. To further concentrate the light on smaller area, the mirrors are often divided into smaller facets that are individually angled in a way that the image of the sun is reflected from each facet to the same spot on the receiver as illustrated in Figure 2.10. This is also known as **canting**. In effect this approximates a parabolic mirror. The heliostat illustration in Figure 2.2 also displays this faceted structure. (Richter et al., 2013, 33)
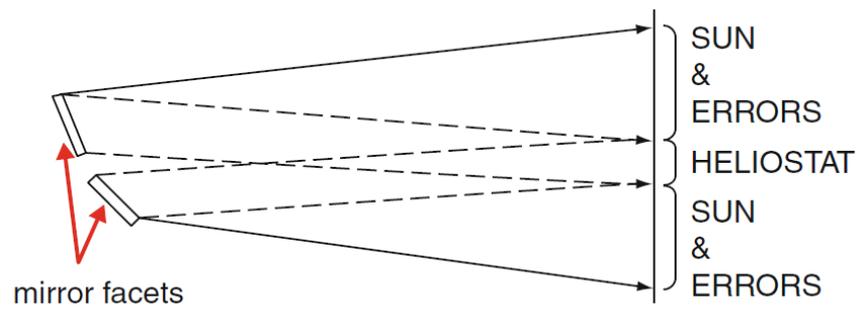
Figure 2.10: Mirror canting. (Richter et al., 2013, 34)

Canting is usually done permanently in a fixed frame, and cannot be adjusted during normal plant operation. Fixed canting has the disadvantage that it can only be done accurately for certain sun position. When solar radiation arrives at the canted mirror in a non-ideal angle, the reflected image is distorted, and does not form a perfect spot on the receiver as illustrated in Figure 2.11. This effect is referred to as off-axis aberration. (Richter et al., 2013, 33-34)
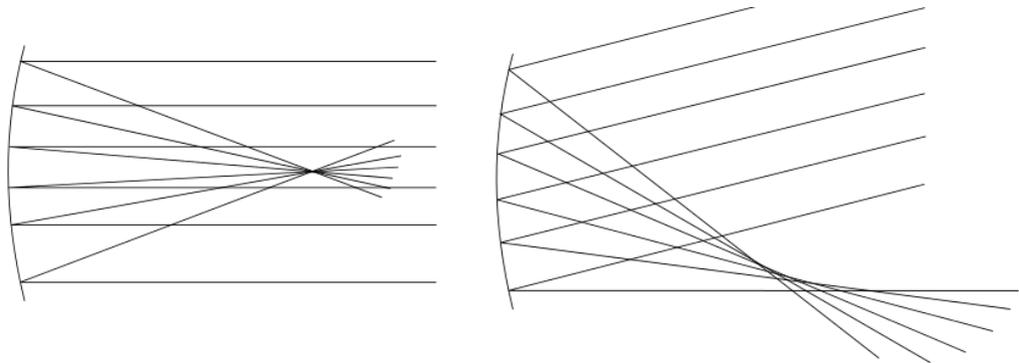
Figure 2.11: Off-axis aberration on a parabolic reflector. Left: on-axis light is reflected to a sharp focal point. Right: off-axis light does not converge to a perfect focal point.

Off-axis aberration has an effect on the power distribution on receiver surface, and can lead to higher spill losses, if mirror placement and canting is done unfavorably. Therefore the tools used to model heliostat fields must be able to take it into account.

Cosine loss is one of the most significant losses in the solar process. As each mirror is angled to allow light to reflect toward the receiver, the effective area of each mirror is reduced proportional to the cosine of the angle between heliostat normal and the sun beam.
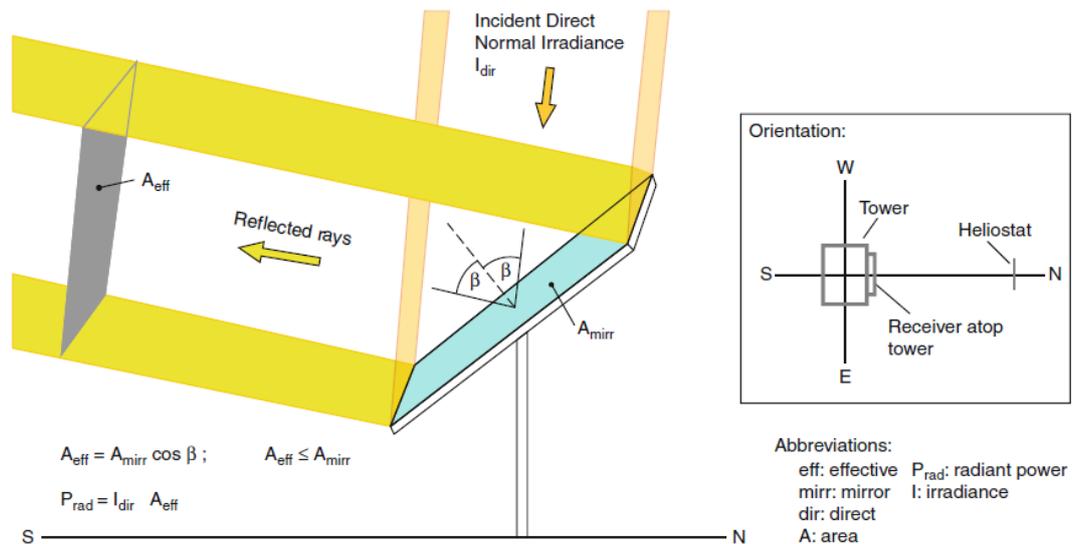
Figure 2.12: Cosine loss. Effective area of the mirror is reduced proportional to the cosine of the angle β. (Richter et al., 2013, 38)

2.2 Existing central receiver technologies

Central receiver plants exist in wide range of scales from few megawatts to several hundred megawatts. Table 2.1 shows a listing of some of the existing and planned central receiver power plants. The listing is not exhaustive and only serves to illustrate range of power plant sizes and heat transfer media. Largest central receiver plant is currently operating in Ivanpah, California and plants of comparable size are under construction in China, South Africa and Chile.

Both steam and salt are commonly used as heat transfer fluids, but molten salt has gained popularity due to good heat transfer properties and the ability to use thermal energy storage.

Table 2.1: Some existing and planned facilities. Power is the nominal electrical power in megawatts.

	Location	Power (MWe)	HTF	Storage	Completed
Copiapó	Chile	260	Molten salt	Yes	?
Redstone	South Africa	100	Molten salt	Yes	2018*
Delingha	China	270	Molten salt	Yes	2017*
Ivanpah	California	377	Steam	No	2013
Greenway mersin	Turkey	5	Steam	No	2013
Crescent Dunes	Nevada	110	Molten salt	Yes	2013
Gemasolar	Spain	19.9	Molten salt	Yes	2011
PS20	Spain	20	Steam	No	2009
PS10	Spain	10	Steam	No	2007

*estimate

Most commonly the mirrors are arranged in radial pattern around the receiver, surrounding the receiver partially or entirely. On the Earth's northern hemisphere, fields are commonly arranged on the norther side of the receiver, since field efficiency is the highest in this configuration. The fields of the Spanish Planta Solar facilities are arranged this way as seen in Figure 2.13. Similarly south field is the most optimal on the southern hemisphere. Surrounding field is most optimal close to the equator where the sun shines directly overhead most of the year. The difference between north and surrounding fields becomes greater when moving to higher latitudes, as the sun shines at steeper angles, and parts of the field is forced to reflect the light at unfavourable angles.

Figure 2.13: Planta Solar power plants PS10 and PS20 with north field (Müller-Steinhagen,2013,13)

However, overall cost of construction needs to be considered in deciding field layout. Greater performance may be achievable with surrounding field even when north field would theoretically be more optimal, because a single receiving tower can be used with larger number of heliostats using a surrounding field, lowering the costs. Local light attenuation and spill losses also become a limiting factor in a large north field, as the farthest mirrors operate suboptimally. The Crescent Dunes power plant seen in Figure 2.14, as an example, is situated in comparable latitudes as Planta Solar and uses surrounding field instead of north field configuration.

Figure 2.14: The Crescent Dunes solar thermal power plant (Solar Reserve)

Current commercial solar projects are focused primarily on large plants with very large unit size as seen in Table 2.1. This has the clear disadvantage of long construction times and difficulty in estimating costs and performance. Some interest exists for smaller scale facilities such as the Greenway Mersin power plant in turkey and markets exist for smaller companies. Esolar in particular uses decidedly smaller towers and fields focusing instead on lowering costs by simplifying construction and high volume manufacturing of the power plant components. These plants are to be constructed modularly in required quantities to accommodate any plant size, while keeping the costs more predictable than large unit installations. Figure 2.15 shows the small scale units of the Sierra Suntower demonstration facility. (Schell, 2011, 614)

Figure 2.15: Sierra Suntower demonstration facility, Lancaster, CA, USA. (Schell, 2011,615)

2.2.1 Receivers

At the focus point of the collector is the receiver. A simple receiver consists of vertical pipes arranged into a membrane wall in shape of a plane or a cylinder. Heat transfer fluid is passed through the pipes where it heats up to a high temperature. If water is used as the fluid, portion of the pipes can be used as boilers and others as superheaters. Many solar projects have opted to using molten salt as HTF, which makes receiver construction and operation simpler as there is no phase change happening inside heating tubes. This configuration requires separate steam generator for the power conversion.

Cavity receiver encloses high temperature surfaces onto a cavity with a smaller aperture area without trading off absorber surface area. Small aperture leads to smaller emission and convection losses on the receiver. Cavity receiver is structurally more complex than external receivers, which will increase receiver construction cost, but higher efficiencies can lead to smaller required collector area, resulting in savings from other parts of the project. Cavities can be only partial such is the case with the PS10 project (Romero-Alvarez & Zarza, 2007, 77), wherein simpler cavity construction is used to gain moderate increases in receiver efficiency.

Cavities can be open to the atmosphere, i.e. there is no window in the aperture, and light can enter the cavity unobstructed. Radiation losses remain low, but in strong wind conditions there can still be convection losses through open apertures. Fully closed cavity has negligible convection losses caused by wind, but they must have a transparent window that can pass high solar fluxes through, which increases the size and mass of the receiver. Windowed receiver can be pressurized, which increases heat transfer properties in cases where gas is used as heat transfer medium. Higher temperatures can be used as well, which allows using Brayton cycle gas turbines in a combined cycle power plant. Figure 2.16 shows a pressurized cavity receiver with a volumetric absorber. This concept has been demonstrated at Plataforma Solar de Almería at temperatures up to 1050 °C and pressures up to 15 bar, with 230 kW output power. (Müller-Steinhagen,2013,13)
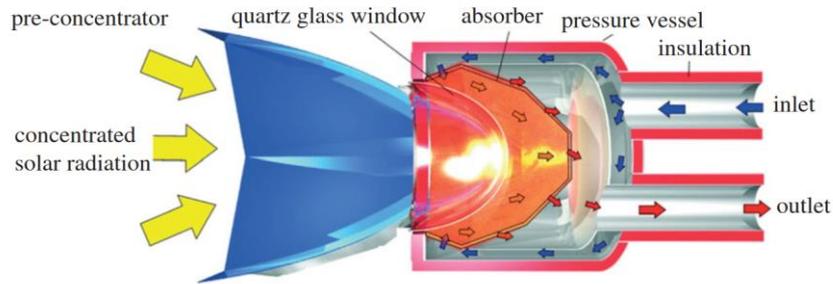
Figure 2.16: Pressurized volumetric cavity receiver (Müller-Steinhagen,2013,13)

Volumetric receivers work by drawing in gas through porous ceramic material as illustrated in Figure 2.17. The gas can be air directly from atmosphere, or any suitable gas contained within the receiver loop, if the receiver is closed to the atmosphere. Ceramic materials can withstand higher temperatures than metallic receivers, but have poorer heat conduction properties through the material. In a volumetric receiver, airflow through the porous material aids in keeping the bulk of the material at more uniform temperature even deeper behind the surface, which greatly increases the heat transfer contact area. This allows more gas to be passed through the receiver and also increases the structural durability under varying conditions.
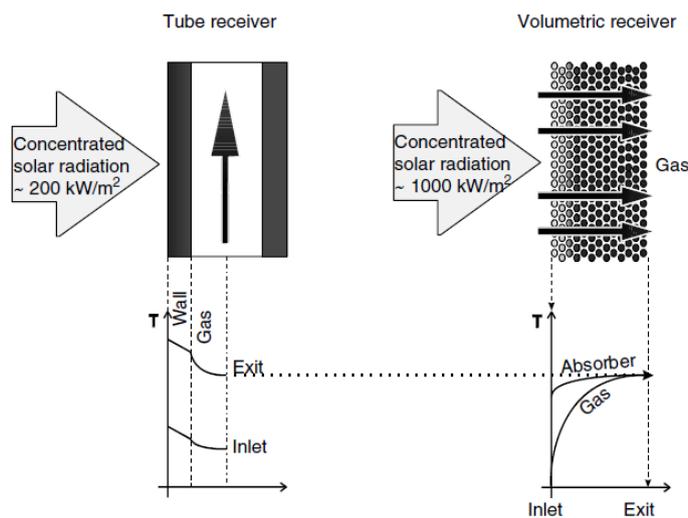
Figure 2.17: Temperature distribution of tube and volumetric receiver surfaces (Romero-Alvarez & Zarza, 2007, 64)

3. EXISTING CENTRAL RECEIVER MODELLING TOOLS

The development effort included a survey of existing tools suitable for central receiver modelling. Primary intent of the survey was to get a good picture of what is generally achievable with the current state of technology, and to establish suitable development targets for the presented model. As mentioned in chapter 1.2, preliminary goals also included the possibility of integrating existing tools into Apros modelling. While this was eventually deemed infeasible, the following selection of tools reflect this consideration to an extent.

There exist a large number of different software for CSP modeling in the industry, however only few of these are publicly available and yet fewer are suitable for modelling central receiver systems. Four programs were selected for closer inspection. Although none of them influenced the presented model implementation directly, the experiences gained from the survey were utilized in user interface design and overall usability considerations.

3.1 DELSOL

Delsol is a fast analytical approximation tool for optimizing central receiver plant designs, developed by Sandia National laboratories (Kistler, 1986, 3). Originally it was developed to quickly optimize designs to sufficient precision with limited computational power. It is still in use today, but has lost some of the original advantages, as computational power has increased and new techniques have been developed for central receiver modelling.

Delsol has no graphical user interface, and is entirely configured by text files. Although the configuration options are extensive, they are still limited to modeling certain types of field configurations.

3.2 Soltrace

Soltrace is a proprietary ray tracing code developed by the National Renewable Energy Laboratory (NREL) of the United States, and is freely available for download (NREL website). Soltrace uses the Monte Carlo approach for ray tracing, in which random selection of rays are cast from infinity against the scene geometry and traced through number of reflections and refractions. This has the advantage of very accurately representing physical light interactions, but this accuracy comes with significant computational cost. This makes it impractical for high performance simulations. The Soltrace code has been validated against measurement data from the NREL's High Concentration Solar Furnace (Wendelin, 2003)

Soltrace has a very simple intuitive user interface, saving considerable amount of time on initial set up for incidental use. This has likely contributed to Soltrace's success as a point of reference for other models. The system includes a simple internal scripting language for task automation. Soltrace's simple scene file format also lends it for use with externally controlled tasks. While this would make it suitable for use with Apros simulations, the computational requirements are prohibitively high in most cases.

3.3 Tonatiuh

Tonatiuh is an open source Monte Carlo ray tracer for concentrated solar power applications, originally funded and developed by NREL and CENER (Centro National de Energías Renovables) the Spanish national renewable energy centre. In terms of functionality, Tonatiuh is very similar to Soltrace, and has the same advantages and disadvantages. (Tonatiuh website)

Tonatiuh also contains an internal scripting language for automation tasks. The user interface is considerably more robust than in Soltrace, which potentially makes it a more powerful tool for modeling complex reflectors. The open source nature of Tonatiuh would make it possible to adapt it for the purposes of Apros simulations, but similarly to Soltrace the computational requirements are too high for extensive use. (Tonatiuh website)

3.4 HOPS

HOpS or Heliostat Optical Simulation is developed as part of the RE<C initiative (Renewable Energy cheaper than Coal) by Google. HOPS was initiated with very similar motivations as this thesis work. Namely it attempts to find a middle ground between the speed of analytical approximations and the accuracy of ray tracing, as suitable software tools are not readily available. (Google HOpS documentation)

Of all reviewed software, HOPS appeared to be best contender for potential integration with Apros simulations, but at the time of writing it appears to not be mature enough to be relied on, and its long term development is uncertain.

4. MODELLING OF CENTRAL RECEIVER SYSTEM

Physical phenomena relating to central receiver systems were discussed in chapter 2. This chapter explores these physical principles from a mathematical and computational stand point, and presents efficient implementations for each part of the model. Some physical phenomena can be expressed mathematically in a simplified manner, allowing more efficient computation. Simplifications may affect accuracy or applicability of a model, but the efficiency tradeoff is often justified.

The presented model is intended primarily for modeling central receiver systems. In principle, it is also capable of modeling parabolic troughs and linear Fresnel collectors, but at the time of writing the implementation does not efficiently support such configurations and the included configuration utility is not suitably equipped to represent them.

As discussed in previous chapters, the presented solar power plant process can be thought of consisting of three distinct components, which can be considered independent of each other: The collector, the receiver and the power conversion process. The collector and the receiver have been implemented as computational modules, which work along with Apros. Due to computational requirements, the collector model is implemented in high performance C-code running in separate process, whereas the receiver model is simple enough to run in real time within the Apros process. Small section of a steam loop in Apros is presented as an example, but full power conversion process is not considered in this thesis. This is sufficient to prove the practical applicability of the model.

Because of computational and algorithmic complexity, the collector model required the majority of the development time and is presented in greatest detail in this chapter. Model choices and implementations in program code have been such that further improvements in the code can be made with ease.

4.1 Collector

The chosen collector model is in large part based on a computational model described in (Noone et al. 2012). This model uses simplified ray tracing to produce good approximation of the result while reducing the computational requirements significantly. Regular Monte Carlo ray tracing is generally more accurate, but requires significantly more computational power due to larger number of rays that need to be traced. Selected model uses several approximations and assumptions to reduce the computational requirements enough to make the model efficient enough for use in cases where large number of simulations need to be run in varying operating conditions.

The implemented heliostat field model takes into consideration all the necessary losses including atmospheric losses, cosine loss, local atmospheric attenuation, reflectance, blocking and shading, and spill losses. Computationally it is more convenient to consider the losses by their respective efficiencies. All the losses for the collector can be summarized with the equation for total collector efficiency

$$\eta_{\text{tot,col}} = \eta_{\text{atm}}\, \eta_{\text{cos}}\, \eta_{\text{att}}\, \eta_{\text{refl}}\, \eta_{\text{block}}\, \eta_{\text{shade}}\, \eta_{\text{spill}} \qquad (2)$$

The efficiencies are in order: atmospheric, cosine, attenuation, reflection, mirror blocking, mirror shading and spill efficiency. Each of these losses is explained in detail in this chapter. However, this is an idealized representation, which does not exactly match the discrete ray tracing implementation. The computational model only has to consider few of these explicitly as some losses emerge naturally from the ray tracing process. The output of the ray tracer is calculated cumulatively and some losses take effect by omitting rays from the result. Representation of the same equation more closely matching the implementation is later given in equation (27), once more context has been provided.

Two different models are used to model light transmitting through the atmosphere. Global atmospheric loss η_{atm}, i.e. the loss happening as radiation travels from space through the atmosphere, is handled by existing Apros module and its implementation is not part of this thesis work. Some details concerning the atmospheric loss model

are still discussed in section 4.2. Model for calculating the local attenuation η_{att} is described in chapter 4.3.

Cosine loss happens as the apparent mirror area facing the sun gets smaller as the mirror tilts away from the sun. Figure 4.1 illustrates the difference in the amount of radiation landing on a horizontal surface as opposed to a surface perpendicular to the solar beam normal. The loss is proportional to the cosine of the angle between solar direction and the heliostat normal. This is also equivalent to the dot product of the respective unit vectors as shown in equation (3).

$$\eta_{cos} = \cos\theta = \boldsymbol{n}_{sun} \cdot \boldsymbol{n}_{hs} \tag{3}$$
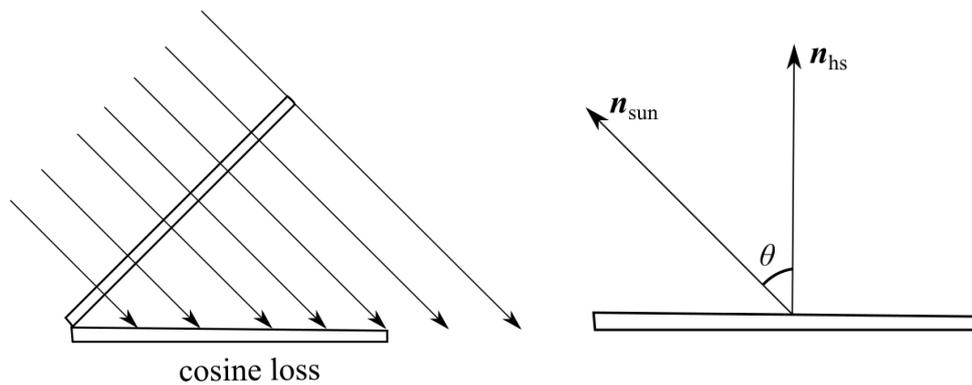
cosine loss

Figure 4.1: Cosine loss. Apparent area of the heliostat surface is reduced proportional to the angle between the solar direction and heliostat normal.

Chapter 2.1 discusses light spreading due to surface imperfections, sun shape and environmental conditions. This spread is modeled by enveloping each reflected ray with an error cone, whose opening angle represents the uncertainty of the ray's travel direction. As the ray propagates farther from the mirror, its power is spread on wider area. The radiant power distribution reaching the receiver is calculated as the intersection between the error cone and the receiver aperture plane. This way a single ray can represent phenomenon that would otherwise require large number of individual rays. This is elaborated later in this chapter. Ray's behavior is illustrated in Figure 4.2.
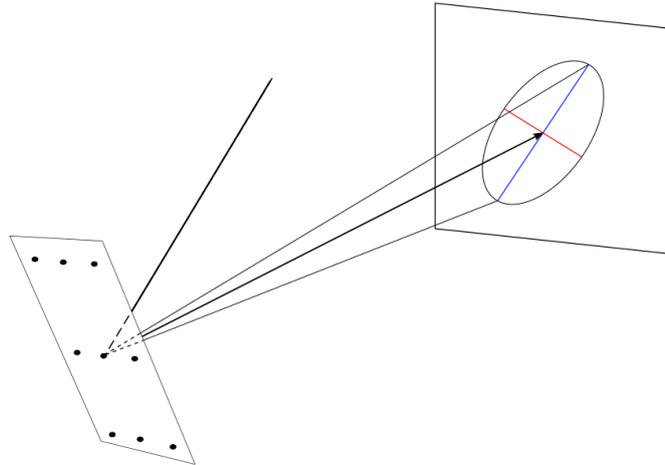
Figure 4.2: Error cone of a reflected ray. Intersection between the cone and the surface represents a radiation flux distribution.

There are several factors affecting the direction of reflected ray. Large mirrors inevitably have microscopic imperfections and larger scale manufacturing defects including canting errors, which can divert rays of light away from the ideal reflection heading.

The sun is not a point source, but has an apparent disc shape. The model considers the radiation intensity distribution across the disc to be normally distributed. Although more accurate sun shape models exist (Buie & Monger, 2004) and the shape can vary over time, assuming a constant normal distribution does not cause large error, and its use is more straightforward in the model.

For simplicity, prior to hitting the mirror the rays are considered parallel to each other traveling in a straight line as if the sun was a point source infinitely far away. Although in reality the sun shape causes some spreading of the light, this causes only negligible error in mirror shading calculations and can be ignored. The directional spreading is instead added to the reflected light error cone, where it is a significant factor in the spill loss computation. Full error cone spread angle is calculated by equation (4)

$$\sigma_{tot}^2 = \sigma_{slope,effective}^2 + \sigma_{sun\ shape}^2 \tag{4}$$

where $\sigma_{slope,effective}^2$ is the effective slope error described by equation (1) and $\sigma_{sun\ shape}^2$ is the spreading caused by sun's apparent shape.

Care should be taken when defining the surface errors since different implementations may use different approaches. SolTrace, as an example, treats macroscopic slope error as deviation of the surface normal, which causes doubled error to the ray direction. Alternatively the slope error can be defined as the deviation of the reflected ray. The final value should be the same in either case, but correct definitions of the input values must be considered.

In the presented model, each ray has certain power proportional to the area of the mirror facet it is calculated from. Spill loss occurs when a representative ray is unimpeded by other heliostats, but some of the ray's energy misses the receiver surface and as a result does not contribute to the irradiation. The intersection between the ray's error cone and receiver aperture plane is a bivariate normal distribution representing the radiant power distribution on the receiver. If the ray arrives at an unfavorable angle, some of the ray's power distribution can lie outside the receiver geometry as seen in Figure 4.4. To get the effective contribution for each ray, the distribution function needs to be integrated over the receiver surface.


Missed radiation
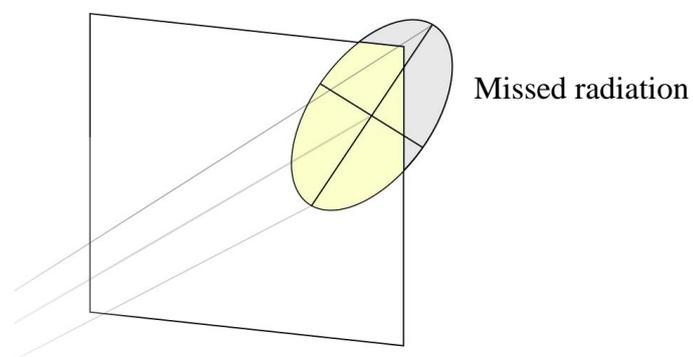
Figure 4.3: Partial spilling of the ray's power.

Analytical integration methods exist in literature (Noone et al. 2012. 796), but they impose certain assumptions on receiver geometry and cannot be used to compute accurate power distribution over the surface. A numerical Monte Carlo approximation method was implemented instead. A good approximation of the true value can be computed by sampling random points from the power distribution at the receiver surface.

$$\boldsymbol{p} = \boldsymbol{p}_0 + \boldsymbol{a}_{\text{major}} \cdot r_1 + \boldsymbol{a}_{\text{minor}} \cdot r_2 \tag{5}$$

Where $\boldsymbol{p}_0$ is the ray hit point and r_i is normally distributed random variable. Vectors $\boldsymbol{a}_{\text{major}}$ and $\boldsymbol{a}_{\text{minor}}$ are the major and minor axes of the normal distribution as illustrated in Figure 4.4.

If the generated point $\boldsymbol{p}$ falls outside the bounds of the receiver surface, it is not counted as contributing to the irradiation. The spill efficiency can then be calculated for a single ray as the ratio of successful hits to total sample size.

$$\eta_{\text{spill,ray}} = \frac{n_{\text{mc,hits}}}{n_{\text{mc,tot}}} \tag{6}$$

Following this principle, only one full ray intersection has to be calculated with the receiver to get sufficiently accurate representation of the amount of radiation contributed by a ray. Only a small number of sample points are needed to get good approximation of the total radiant power at the receiver aperture, as the number of rays overall is sufficiently high to get coverage of sample points falling inside and outside the aperture. Precise calculation of a single ray power distribution is not vitally important since the results only have to be correct on average.
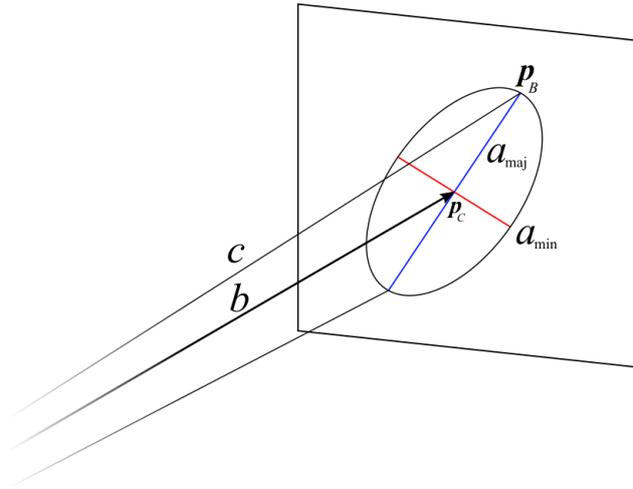
Figure 4.4: Intersection of the ray error cone and the receiver plane. The intersection is a bivariate normal distribution representing the radiation intensity distribution. The axis vectors a_i are the eigenvectors of the corresponding covariance matrix. Black ellipse represents the equivalent of standard deviation distance on 2-dimensional plane.

In the presented ray tracing scheme, rays don't have a clear starting point. The tracing process is started from each of the mirror facets, which is the point of first reflection of the ray. A ray is cast in two directions, toward the sun and toward the receiver. This is done to determine whether the ray has a clear path between the sun and the target. That is, whether another heliostat shades the incoming rays, or if one blocks the reflected ray before it can reach the receiver. Blocking is illustrated in Figure 4.5. Shading works in similar manner, but with reversed ray direction. Mirror shading and blocking is the most computationally intensive part of the model. The calculations are fairly simple, but the sheer amount of needed intersections makes efficient implementation challenging.
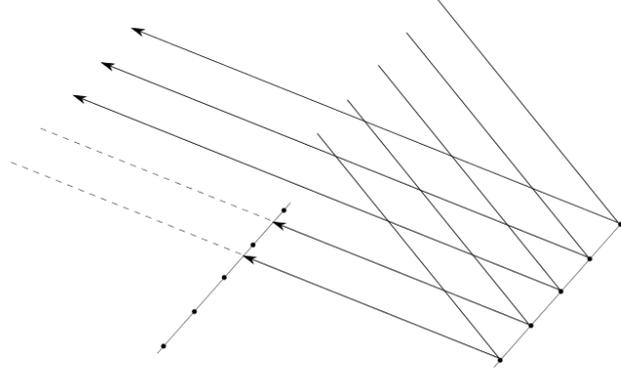
Figure 4.5:   Mirror blocking. Reflected solar rays are blocked by nearby mirrors before they reach the receiver.

An intersection between a heliostat plane and a ray of light is computed as a simple ray-plane intersection with equations (7), (8) and (9). The geometry and notation is illustrated in Figure 4.6. Starting from point $\boldsymbol{p}_0$ at the first heliostat surface, perpendicular projections d_{r1} and d_{r2} are calculated by dot products against the target heliostat normal. The travel distance of the ray is the ratio between these projections. Final point is obtained by shifting the starting point by this distance in the direction of the ray heading.

$$d_r = (\boldsymbol{p}_{\text{hs2}} - \boldsymbol{p}_0) \cdot \boldsymbol{n}_{\text{hs2}} \tag{7}$$

$$d_{r2} = \boldsymbol{n}_{\text{hs2}} \cdot \boldsymbol{u}_{\text{r}} \tag{8}$$

$$\boldsymbol{p}_{\text{hit}} = \boldsymbol{p}_0 + \frac{d_r}{d_{r2}} \boldsymbol{u}_r \tag{9}$$

$\boldsymbol{p}_0$ is the starting point at first heliostat surface

$\boldsymbol{p}_{\text{hs2}}$ is the pivot point of the target heliostat

$\boldsymbol{u}_{\text{r}}$ is ray direction unit vector

$\boldsymbol{n}_{\text{hs2}}$ is target heliostat normal

d_{r1} and d_{r2} are scalar projections
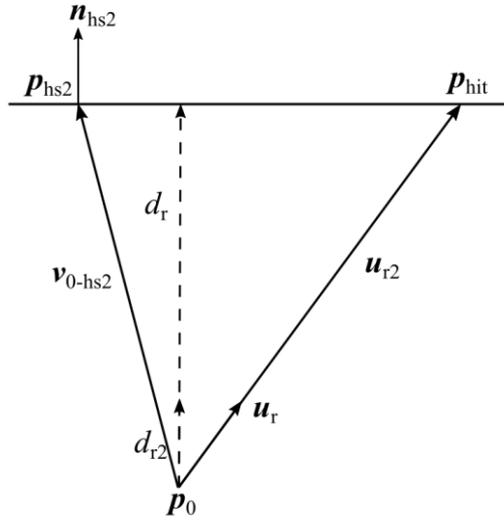
Figure 4.6: Ray intersection with a heliostat plane

To determine whether the ray hit the heliostat plane within the bounds of the mirror, scalar projections are also calculated against the heliostat width and height axes.

The power distribution axis vectors are also calculated with simple trigonometry. For simplicity, the cone axis was assumed to pass through the intersection ellipse center point. This is not exactly true in reality, but the error this simplification causes was deemed to be very small on average. The following calculations use the notation in Figure 4.7.

Cone opening angle is the total error of ray direction defined earlier in equation (4)

$$A = \sigma_{tot} \tag{10}$$

The angle C can be calculated based on the angle between the receiver surface normal and the ray heading.

$$C = \mathrm{acos}(\boldsymbol{n}_{hs} \cdot \boldsymbol{u}_{b}) + \frac{\pi}{2} \tag{11}$$

Angle B can be found based on other triangle angles.

$$B = \pi - A - C \tag{12}$$

Using law of sines, the major axis a can now be computed

$$\frac{b}{\sin B} = \frac{a_{\mathrm{maj}}}{\sin A} \tag{13}$$

$$a_{\mathrm{maj}} = \frac{\sin A}{\sin B} b \tag{14}$$
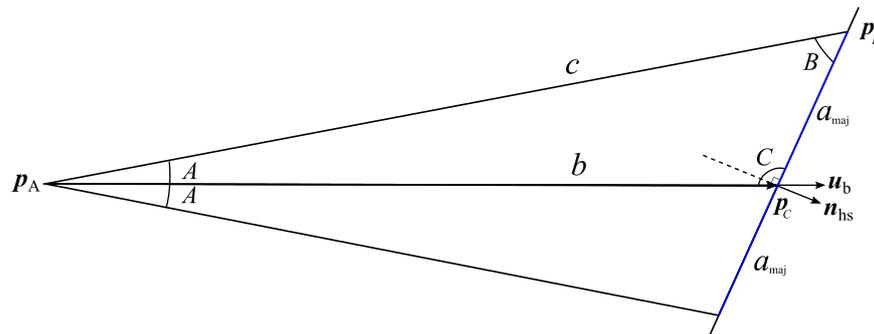
Figure 4.7: Side view of the cone intersection. View from different angle with equivalent notation can be seen in Figure 4.4.

Minor axis is simply the vector perpendicular to the major axis with a length defined by the equivalent triangle of the opening angle by equation (15). Illustration can be seen in Figure 4.8.

$$a_{\mathrm{min}} = b \cdot \tan A \tag{15}$$
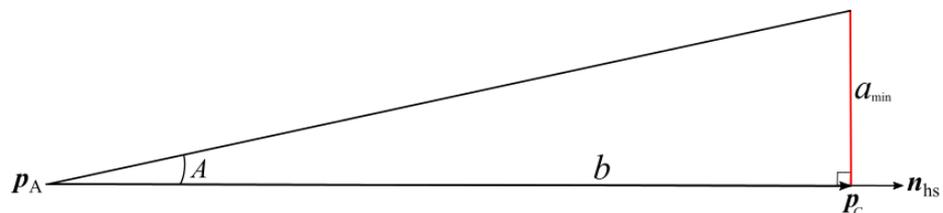
Figure 4.8: Top view of the cone intersection. View from different angle with equivalent notation can be seen in Figure 4.4.

The second supported receiver primitive shape is a cylinder. Two different intersection methods are implemented: a fast planar projection and full ray-cylinder intersection. The fast projection is done for the benefit of spill loss calculation as it can be calculated with the same equations as the planar intersection. The fully accurate intersection is added for future benefit in case situations arise, where the projection method does not suffice. However, the planar error cone intersection approximation does not work accurately with cylinder geometry, so multiple ray-cylinder intersections would have to be calculated to get the same accuracy.

The planar projection method (Figure 4.9) was developed because the error cone intersection against a cylinder is considerably more involved to calculate if done naïvely, and would require significantly more computing power than the equivalent calculation against a plane receiver. The Monte Carlo sampling is done against a plane whose xy-direction is set perpendicular to the ray. Additionally the cylinder's clipping boundary is reduced to a simple equation of a circle in Cartesian coordinates.

Justification for both of these conditions is that all ray origins are sufficiently far away to consider the tower essentially a flat plane when viewed along the ray's path. The plane has width equivalent to the cylinder diameter, and clipping boundaries shifted by an elliptical arc due to view angle distortion of the circular cylinder rim. The cone spread is also considered negligible over the width of the cylinder, i.e. the cone-cylinder intersection is approximately cylinder-cylinder intersection.
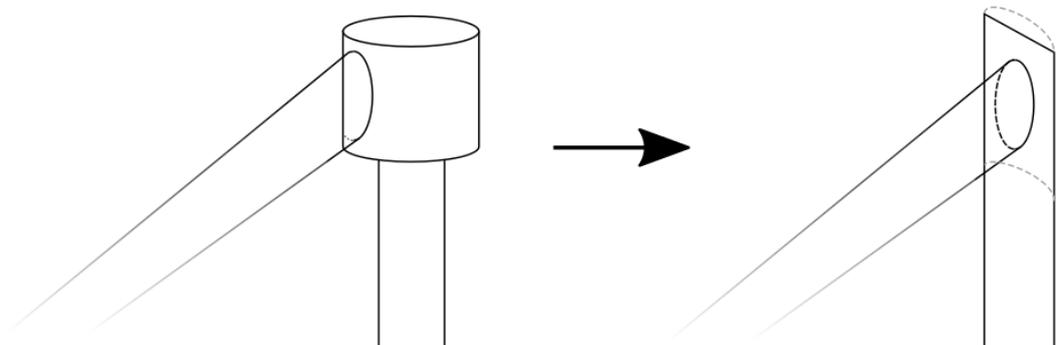
Figure 4.9: Conversion of cylinder receiver to a plane approximation.

Every point of the cone intersection is calculated on the plane in the same way as with the basic plane receiver, but the view angle distortion caused by the cylinder receiver's curved surface is taken into account by vertical shift calculated with equation (17). The calculations use notation in Figure 4.10 and Figure 4.11.
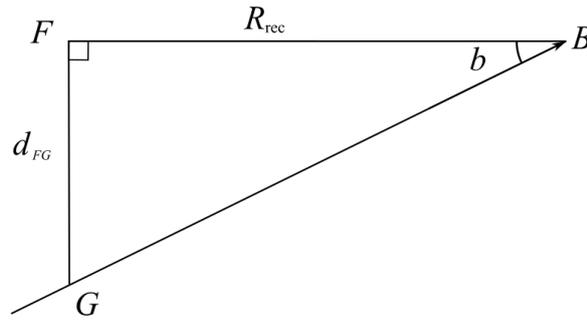
Figure 4.10: Side view of the cylinder projection definition
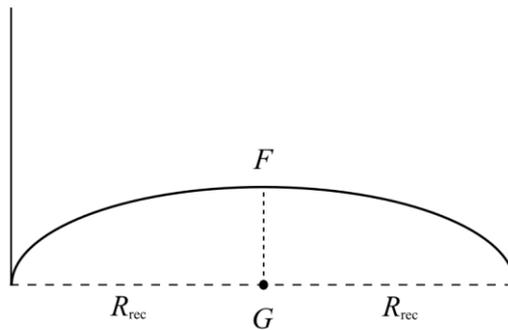
Figure 4.11: Cylinder projection as viewed along the line $\overline{GB}$

Magnitude of the view distortion is determined by the angle b between horizontal plane and the vector from ray origin to the lowest middle point of the receiver. The highest point in the projected circle d_{FG} is defined by equation (16).

$$d_{FG} = R_{\text{rec}} \tan b \tag{16}$$

The vertical shift at any point along the width of the receiver is then calculated by equation (17).

$$y = d_{FG}\sqrt{R_{rec}^2 - x^2} \tag{17}$$

The fully accurate intersection is done much the same way as with a plane, with simple trigonometry and vector arithmetic. Analytical cylinder-line intersection equation can be derived (Zorin, 1999, 3), but in this case it is more convenient to derive a step-by-step procedure based on the geometry, as the solution is more easily understood and simple to implement in the case where initial values are already in vector form. Figure 4.12 shows a top-down view of the ray-cylinder intersection and equivalent side view is shown in Figure 4.13. Point A marks the ray origin, E is the final intersection point and B is receiver center point. The vector r is the 2-dimensional projection of ray travel direction as unit vector.
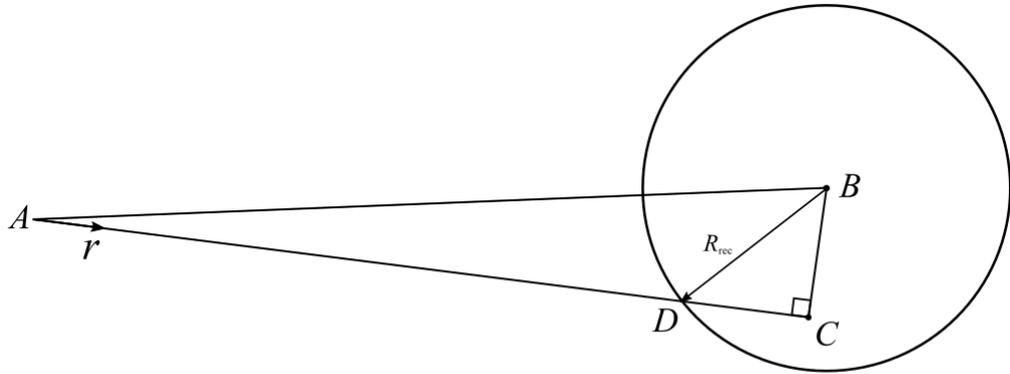
Figure 4.12: Top-down view of ray-cylinder intersection. Vector r is the normalized 2D-projection of the original ray.

First define the vector from A to B.

$$\boldsymbol{v}_{AB} = B - A \qquad (18)$$

Distance from A to C is calculated as a scalar product of $\boldsymbol{v}_{AB}$ against the 2-dimensional direction vector r.

$$d_{AC} = \boldsymbol{r} \cdot \boldsymbol{v}_{AB} \qquad (19)$$

Vector from A to C is then calculated by equation (20) and point C by equation (21).

$$\boldsymbol{v}_{AC} = \boldsymbol{r} \cdot d_{AC} \qquad (20)$$

$$C = A + \boldsymbol{v}_{AC} \qquad (21)$$

The perpendicular distance from B to C is determined by equation (22)

$$d_{\mathrm{BC}} = |B - C| \tag{22}$$

If distance d_{BC} is greater than the receiver radius, the ray has missed. The distance from C to D can then be calculated by simple Pythagorean relation. The distance from A to D is then determined by simply subtracting the known distances by equation (24).

$$d_{\mathrm{CD}} = \sqrt{R_{\mathrm{rec}}^2 - d_{\mathrm{BC}}^2} \tag{23}$$

$$d_{\mathrm{AD}} = d_{\mathrm{AC}} - d_{\mathrm{CD}} \tag{24}$$

The point D can now be calculated by equation (25).

$$D = A + \mathbf{r} \cdot d_{\mathrm{AD}} \tag{25}$$

The actual hit point E on the receiver (Figure 4.13) is calculated by proportional distance in relation to the 2D-intersection by equation (26).

$$E = \frac{d_{\mathrm{AD}}}{|\mathbf{r}_0|} \cdot \mathbf{r}_{\mathrm{ray}} \tag{26}$$

Additionally checks are made to determine if ray has hit over or under the receiver bounds. In those cases ray is considered to have missed.
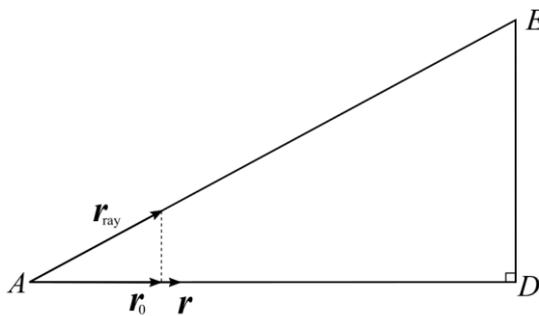
Figure 4.13: Side view of the ray-cylinder intersection.

This computation assumes that cylinder is aligned vertically. Cylindrical receivers are mounted in vertical orientation in the majority of cases so this is a safe assumption. Should the need arise to implement non-vertical orientation, it can be easily achieved with basic coordinate transformations without changing the underlying algorithm.

In naïve implementation an intersection must be computed against every heliostat to test whether the ray reaches the receiver. This has worst case compute time scaling proportional to the square of the number of heliostats. This is clearly not feasible for larger plants with tens of thousands of heliostats, and optimization must be considered during development.

To avoid calculating intersections unnecessarily an optimization grid is defined. The heliostats are added to the grid wherever their bounding box intersects with the grid cells, as illustrated by Figure 4.14. Each heliostat has a bounding box that is defined by the turning radius of the heliostat. Rays traverse the grid one cell at a time, and only test intersection with the heliostats within each grid cell they enter. If there are no heliostats in a cell, no computations are done and the ray moves to the next cell. Using a grid, the computational time is linearly proportional to the number of heliostats.
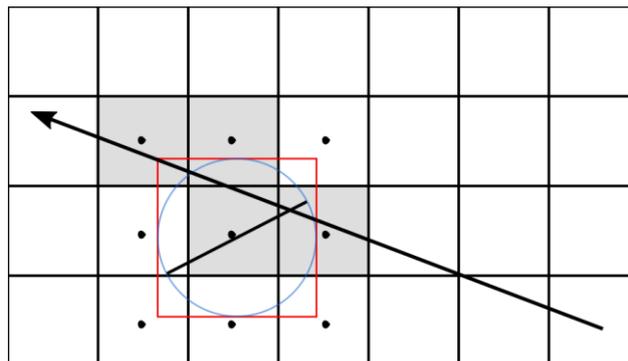
Figure 4.14: The 2D grid for ray intersection optimization. The black arrow represents the traced ray, the black line is the heliostat, the blue circle is the bounding circle and the red rectangle is the bounding box. The black dots indicate grid cells where the heliostat is considered during calculation, and the shaded cells are cells where computations for the passing ray are performed. Calculations are not performed in white cells.

As the ray traverses the grid, each time a possible intersection is detected, a full intersection is calculated. If a hit is not found, the grid traversal continues. Compared to the intersection testing, the grid traversal calculation causes very little computational strain. The implementation is based on (Amanatides & Woo, 2010), but the implementation details fall outside the scope of this thesis. Alternatively any grid traversal algorithm can be used as effectively.

For convenient interoperability with other Apros solar simulation modules, the output of the heliostat model was chosen to be an effective representative collector area at a given time, which is returned to the Apros simulation acting as a multiplier for direct beam irradiance. The area includes the area of all facets that have clear path between the sun and the receiver and all relevant losses have been added as multipliers.

$$A_{\text{eff}} = \sum_{i=1}^{n_{\text{hs}}} \eta_{\text{att,i}}\, \eta_{\text{refl,i}} \sum_{j=1}^{n_{\text{fac}}} A_{\text{f}}\, \eta_{\cos,j}\, \eta_{\text{spill,ray,j}}\, \eta_{\text{block,j}}\, \eta_{\text{shade,j}} \tag{27}$$

Where A_{eff} is effective area (m^2),

   n_{hs} is the number of heliostats,

   n_{fac} is the number of facets on each heliostat,

   A_{f} is the area of a single mirror facet,

   $\eta_{\text{att,i}}$ is the local attenuation efficiency calculated for each heliostat,

   $\eta_{\text{refl,i}}$ is the mirror reflection efficiency,

   $\eta_{\cos,j}$ is the cosine efficiency of j_{th} facet of i_{th} heliostat and

   $\eta_{\text{spill,ray,j}}$ is the portion of a ray's power that reaches the receiver

$\eta_{\text{block,j}}$ and $\eta_{\text{shade,j}}$ are always either 0 or 1 based on whether the ray has been blocked or shaded. Equation (27) matches the actual implementation in code more closely than the idealized efficiency presented earlier in equation (2).

Irradiation power reaching the receiver surface is thus

$$P_{\text{rec}} = B_c \cdot A_{\text{eff}} \tag{28}$$

where B_c is direct beam irradiance.

4.2   Direct normal irradiance estimation with clear sky model of the ESRA

The presented model can utilize direct beam irradiance measurement data to simulate real world conditions accurately, but often such data is not available. In these cases having ability to calculating a reasonably good estimate is very important. Apros natively contains a process diagram component for modelling solar radiation, which can output direct normal irradiance as numerical value. At the early stages of this thesis work, the quality of the model used by Apros was not known, so a survey of existing models was conducted. The survey concluded, that the existing model is accurate and usable, but its most effective use would require estimation of Linke turbidity factor T_L, which is used as input value. This only requires some calculations to be done before the Apros radiation model component is run, but no changes are needed to the component itself.

The Apros component implementation is known to closely follow the irradiation model implementation of the Geographical Information System (GIS) of the open source Geographical Resources Analysis Support System (GRASS) as described in (Hofierka & Šúri, 2002, 4). This model is based on the clear sky irradiance model for European Solar Radiation Atlas (ESRA) described in (Rigollier et al., 2000).

There currently exists several dozen models for estimating solar irradiance, but there is not any single one best model for all conditions and radiation types (Badescu et al., 2012, 1654). The ESRA clear sky model relies on the availability of Linke turbidity factor data to produce accurate results, which may be problematic, as models that rely on Linke turbidity measurements as an input have not ranked well in performance studies (Badescu et al., 2012, 1654).

A suggested correction for the ESRA model is given in (Badescu et al., 2012, 1638). Rather than obtaining the Linke turbidity factor T_L directly, it is derived as a function of Ångström's turbidity factor β and atmospheric precipitable water vapor content by equation (29). The β coefficient can be derived from measurements of atmospheric optical depth (also referred to as atmospheric optical thickness), which is readily available worldwide through the Aerosol Robotic Network (AERONET) organized by NASA. This correlation was referenced from (Dogniaux,1986) by Badescu, but it

is quoted here via (Page, 1986, 399) and (Gueymard, 2003, 358) due to unavailability of the original source.

$$T_L = \left(\frac{85 + \gamma}{39,5 \; e^{-w} + 47,4} + 0.1 \right) + (16 + 0,22w) \cdot \beta \tag{29}$$

where γ is solar elevation angle (° from horizontal plane),

β is Ångström's turbidity coefficient (unitless),

w is precipitable water content in vertical atmospheric column (cm)

With this correction, the ESRA model has performed very well in performance studies (Badescu et al., 2012). The coefficient β can be calculated from the AERONET measurements by fitting Ångström's law, equation (30), over the data across the whole spectrum.

$$\tau_a(\lambda) = \beta \lambda^{-\alpha} \tag{30}$$

Where τ_a is the atmospheric optical thickness for the wavelength λ,

β is the Ångström's turbidity coefficient,

α is Ångström's exponent

Values for τ_a and λ are obtained from the AERONET measurement data. The factors α and β can be solved by linearization of equation (30), for which simple least squares fitting can be done.

$$\ln \tau_a = \ln \beta - \alpha \ln \lambda \tag{31}$$

In reality α and β depend on wavelength, and the relation is not strictly linear (Kaskaoutis et al., 2007, 7354), but as ESRA and Dogniaux's correlation are broadband approximations, a linear fit over the whole spectrum can be used. User discretion is always advised when estimation functions are used. There still exists a lot of uncertainty in irradiance approximation functions, and measurement data should be preferred when available.

4.3 Local radiation attenuation

In addition to light attenuation in atmosphere, large solar plants must account for attenuation happening between the heliostats and the receiver. In large plants the farthest heliostats can be over a kilometer away and the air mass between them and the receiver will scatter the light to an extent that must be considered in the model.

In contrast to the attenuation model used in (Noone et al. 2012), namely a model by Vittitoe and Biggs (1978), the presented ray tracer implements a model developed by Pitman and Vant-Hull (1982), quoted here via (Cardemil et al., 2014) due to unavailability of the original source.

Inputs of the model are the tower height H_T (km), site elevation H_S (km), atmospheric water vapor content ρ_w (g/m^3), optical visibility V_R (km) and heliostat slant range R (km). Slant range is the shortest distance between the heliostat surface and the receiver, illustrated in Figure 4.15.
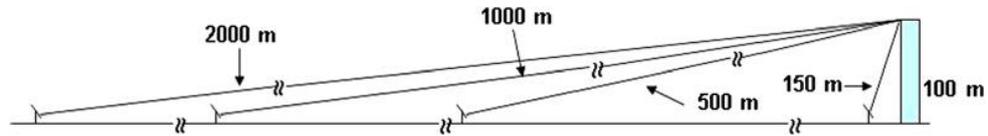
Figure 4.15: Slant range. The shortest free path between each heliostat and the receiver. (Ballestrín & Marzo, 2012, 390)

Equation (32) correlates visibility to a scattering coefficient at wavelength band around 550 nm (Cardemil et al., 2014, 1290). Equations (33) through (38) calculate the attenuation model parameters A, C and S. A is the rate in which the extinction coefficient diminishes with altitude, C is the average extinction coefficient for zero tower height, S is the transmission model exponent (Cardemil et al., 2014, 1291).

$$\beta = \frac{3.912}{V_R} \tag{32}$$

$$C_0 = 0{,}0105\,\rho_w + 0{,}724 \tag{33}$$

$$S_0 = 0{,}00101\, \rho_w + 0{,}0507 \tag{34}$$

$$A_0 = 0{,}0112\, H_S + 0{,}0822 \tag{35}$$

$$C = C_0(\beta - 0{,}0037)^S \tag{36}$$

$$A = A_0 \ln\left(\frac{\beta + 0{,}0003\rho_w}{0{,}00455}\right) \tag{37}$$

$$S = 1 - S_0(\beta + 0{,}0091)^{-1/2} \tag{38}$$

H_S is the site elevation (km) and ρ_w the water vapor concentration (g/m^3). Finally broadband extinction coefficient ξ and the final attenuation efficiency are calculated by equations (39) and (40).

$$\xi = C\, e^{-AH_t} \tag{39}$$

$$\eta_{att} = e^{-\xi R^S} \tag{40}$$

4.4 Receiver

The heliostat field model computes only radiation flux at the receiver surface and only computes losses related to the field. Further heat losses happening at the receiver are handled by a receiver model running within the Apros simulation.

The receiver model is a fast correlation described in (Kim et al. 2015), which is based on CFD simulations of 72 different cases with varying wind conditions and receiver geometry. The model has been validated with multiple empirical data sets (Kim et al. 2015, 321). It is able to model fully external receivers, i.e. planes or cylinders, as well as cavity receivers, which can be partial or full cavities.

The model takes as inputs receiver surface area A_{rec} (m^2), aperture area A_{ap} (m^2), receiver surface emissivity, wind velocity V (m/s), receiver temperature T_{re} (°C) and ambient temperature T_{ap} (°C).

The type of receiver that the input is treated as, depends on the ratio between receiver surface area A_{rec} and receiver aperture area A_{ap}. This is the opening ratio OR described by equation (41).

$$OR = \frac{A_{\mathrm{ap}}}{A_{\mathrm{rec}}} \tag{41}$$

For non-cavity receivers such as planar or cylindrical receivers OR=1. For partial cavity or full cavity receivers OR<1. The model then correlates the opening ratio, wind velocity and receiver surface temperature to a convection factor (FC), which is the ratio of convection loss q_{conv} to the total heat loss q_{tot}.

$$FC = a \cdot \ln(OR \cdot T_{\mathrm{rec}}^4 \cdot 10^{-12}) + b \tag{42}$$

a and b are correlation terms, which are functions of wind velocity V. They are defined by equations (43) and (44). These equations have been derived from the CFD simulation cases.

$$a(V) = -4{,}611 \cdot 10^{-4} \cdot V^2 + 5{,}517 \cdot 10^{-3} \cdot V - 1{,}071 \cdot 10^{-1} \tag{43}$$

$$b(V) = -5{,}917 \cdot 10^{-4} \cdot V^2 + 3{,}158 \cdot 10^{-2} \cdot V + 1{,}190 \cdot 10^{-1} \tag{44}$$

Radiation loss from the receiver surface to the environment is estimated by gray body heat transfer between the surface and the aperture plane, which is treated as a black body at ambient temperature.

$$q_{\mathrm{rad}} = \frac{\varepsilon_{\mathrm{re}}}{(1 - \varepsilon_{\mathrm{re}})OR + \varepsilon_{\mathrm{re}}} \, \sigma\big(T_{\mathrm{re}}^4 - T_{\mathrm{ap}}^4\big) A_{\mathrm{rec}} OR \tag{45}$$

where $\sigma = 5{,}67 \cdot 10^{-8} \frac{\mathrm{W}}{\mathrm{m^2 K^4}}$ is the Stefan-Boltzmann constant

When the radiation loss and the convection factor are known, total heat loss can be found by equation (46).

$$q_{\mathrm{tot}} = q_{\mathrm{conv}} + q_{\mathrm{rad}} = q_{\mathrm{rad}}\left(\frac{FC}{1 - FC}\right) + q_{\mathrm{rad}} = q_{\mathrm{rad}}\frac{1}{1 - FC} \tag{46}$$

Radiative losses are dependent on the receiver temperature. The temperature is affected by the heat exchanger module on Apros' side.

While the model appears to be very widely applicable and accurate within a reasonable tolerance where validation data is available, situations may arise where the correlation cannot be applied. With this in mind, the receiver model has been implemented such that the user can easily implement new case specific correlations when the need arises. Such correlations could be derived from CFD models, as was described in (Kim et al. 2015), or from empirical data when available.

4.5 Model validation

Validating the entire central receiver model as a whole would require sufficiently complete set of experimental data with enough information about the field layout, operating conditions and incident radiation flux on the receiver. It proved challenging to find such comprehensive data set in literature, so each part of the model had to be verified independently from each other.

The correctness of models for local atmospheric attenuation and receiver heat loss are verified with the data in the original papers. In the case of the heliostat field model, i.e. the collector model, a reasonably accurate way to verify correctness is to compare it with other similar program codes that are known to have high degree of physical accuracy. In this case the Soltrace code presented in chapter 3 was used for comparison.

4.5.1 Collector

Correctness of the implementation and physical accuracy is carried out by comparing the results of the ray trace utility to equivalent computation performed using the SolTrace code, which was presented in chapter 3. Both cases use identical heliostat field geometry and environmental properties. The objective was to evaluate the correctness of the radiation model.

The comparison was conducted in fairly idealized conditions, and while the radiation model results are accurate, they are not necessarily intended to match real world

conditions. Receiver reflection, convection and emission losses are not considered, and since Soltrace does not have local attenuation models implemented, attenuation is disabled from the presented model as well for fair comparison. Attenuation could also be accounted for by post processing Soltrace output data with a separate attenuation model, but since the calculations would be identical in both comparison cases, it would not give any additional information.

The comparison test was done by generating solar direction points from a unit hemisphere, where each sample point is a unit vector pointing toward the sun. Full computation of radiation power incident on the receiver was done for each solar direction vector with both models. This approach was intended to reveal any errors which may result from solar direction. However, solar direction does not seem to affect the results, so Table 4.2 shows only a listing of comparison values without the directional information. The procedure would also have revealed any errors or differences in heliostat aiming between the models, had there been any. Input parameters for the model comparison are listed in Table 4.1. The results shown in Table 4.2 display very good agreement between the models.

Table 4.1: Input parameters for the model comparison

Number of heliostats	1036
Field layout	Phyllotaxis pattern based on Fermat's spiral
Mirror width	10 m
Mirror height	10 m
Tower height	115 m
Receiver width	6 m
Receiver height	6 m
Sun shape σ	2,3 mrad
Total slope error σ	2,94 mrad
Direct normal irradiance	1000 W/m^2

Table 4.2: Comparison with the presented collector model and equivalent SolTrace model. Each data point is full computation done with one of 33 solar direction vectors.

Calculated radiation (MW)			Calculated radiation (MW)		
Model	Soltrace	difference (%)	Model	Soltrace	difference (%)
13,57	13,60	-0,3	47,68	48,20	-1,1
22,16	22,40	-1,0	62,05	62,59	-0,9
34,79	35,08	-0,8	74,22	74,88	-0,9
42,26	43,01	-1,7	78,38	79,20	-1,0
44,78	45,37	-1,3	73,43	74,35	-1,2
42,05	42,51	-1,1	61,01	61,61	-1,0
33,78	34,08	-0,9	46,89	47,30	-0,9
21,30	21,30	0,0	52,87	53,14	-0,5
28,09	28,26	-0,6	56,58	57,43	-1,5
38,26	38,45	-0,5	64,71	64,89	-0,3
58,01	58,97	-1,6	71,97	72,51	-0,7
73,87	74,67	-1,1	74,49	74,99	-0,7
78,86	79,96	-1,4	71,38	72,14	-1,1
73,06	74,13	-1,4	63,97	64,51	-0,8
56,78	57,53	-1,3	56,11	56,42	-0,6
37,34	37,39	-0,1	65,81	66,12	-0,5
40,65	40,98	-0,8			

The results can be seen to match very closely, and the sun direction had no effect on the precision of either model. Both of the compared models are probabilistic in nature, so the results can be expected to vary slightly within some tolerance depending on used computational precision. In the given comparison case, the difference is on average 1% with 0,5% sample standard deviation. The presented model gives slightly more conservative results, which is the favourable outcome in case of an error, as this avoids overestimating the simulated power plant's performance.

4.5.2 Receiver model

The receiver heat loss model is based on CFD simulation and has been validated with experimental data of the Solar Two test facility, whose overall performance results are outlined in (Pacheco, 2002). To verify the correctness of the model in the presented implementation, a sample of heat loss values was computed and compared

to the results presented in (Kim et al., 2015, 321). The comparison also includes the experimental data. The results can be seen in Table 4.3, showing good agreement between the two models and the measurement data.

Calculations were done at the temperature 530 °C with a cylindrical receiver with surface area of 99,3 m^2. Reflection loss is not considered in the model, but it is assumed to be 5% by both of the comparison studies (Kim et al.,2012, 321; Pacheco, 2002,111). All model parameters for the comparison calculations were not disclosed, so ambient temperature was assumed to be 25 °C and receiver emissivity $\varepsilon_{rec} = 0{,}75$. Based on the results, these are reasonable assumptions. The results are shown in terms of receiver efficiency for comparison with the available measurement data. The receiver efficiency is calculated as a ratio of absorbed power to the incoming radiation power by equation (47)

$$\eta_{rec} = \frac{q_{in,rad} - q_{loss,tot}}{q_{in,rad}} = 1 - \frac{q_{out,tot}}{q_{in,rad}} \tag{47}$$

where $q_{loss,tot}$ is the sum of radiative, and convective losses and $q_{in,rad}$ is the radiation power incident to the receiver surface.

Table 4.3: Comparison of the presented receiver heat loss model implementation against the original model results and experimental data.

Wind velocity (m/s)	Measured absorber power (MW) (Pacheco, 2002)	Receiver efficiency		
		Measured (Pacheco, 2002)	(Kim et al.,2012)	Presented implementation
0,5	32,4	0,888	0,881	0,881
0,5	34,3	0,88	0,885	0,885
0,8	34,6	0,884	0,885	0,885
0,8	27,7	0,87	0,87	0,869
1,1	28,9	0,871	0,872	0,871
1,2	31,5	0,874	0,878	0,878
1,5	27,7	0,881	0,867	0,867
2,5	31,5	0,866	0,875	0,874
6,4	25	0,856	0,843	0,839

4.5.3 Local attenuation model

Local atmospheric attenuation model was verified using the reference data in (Cardemil et al., 2014, 1293). Numerical data was not provided, so Figure 2 in (Cardemil et al., 2014, 1293) was sampled for data points. Tower height was set to 0,1 km and site is considered to be at sea level (0 km elevation). The results presented in Table 4.4 show very good agreement between the reference data and the model. The remaining error is most likely due to inaccuracies in figure reading.

Table 4.4: Comparison with presented attenuation model implementation and reference model.

	Attenuation (%)			
	visibility water vapor	23 km 11,2 g/m3	visibility water vapor	5 km 19,9 g/m3
Slant distance (km)	Model	Reference	Model	Reference
0,2	4,3	4	14,9	15
0,4	7,7	8	26,3	26
0,6	10,8	11	35,8	36
0,8	13,6	13	43,9	44
1	16,2	16	50,9	51
1,2	18,7	18	56,8	57
1,4	21,0	21	62,0	62
1,6	23,2	23	66,5	66
1,8	25,3	25	70,5	71
2	27,3	27	73,9	74

5. APROS MODEL DEVELOPMENT

To utilize the developed model in practical applications, all the implementations have been tailored to work in conjunction with Apros simulation software. Apros is a dynamic process simulation software capable of fast and physically accurate modelling of real world power plant processes. The models are constructed using primitive components connected together as logically flowing diagrams.

Each individual diagram component contains one or more internal computational components, whose implementations are based on well understood physical principles and empirical correlations. The process components are primarily computed one-dimensionally to keep the processing requirements as small as possible. As a result, the simulations can run tens or hundreds of times faster than real time, which allows different power plant scenarios to be simulated efficiently in a reasonably short time span. Each component carries out its own computations based on its inputs, and the results are passed forward to other connected components. For numerical stability and physical correctness, the parameters for each component have to be carefully considered.

5.1 Implementation of the model in Apros

Mathematical and physical principles of each component of the model are discussed in chapter 4. This chapter expands the implementation details to explain how the computational models are tied to Apros simulations. Part of the receiver model is implemented directly in Apros so some details from chapter 4 are expanded here. The receiver configuration presented here is not feasible from engineering stand point, but gives sufficiently accurate view for correct integration of the receiver model to Apros steam loop. Apros implementation of the collector, i.e. the heliostat field, only presents efficient use of the external model as all model details have already been covered.

The collector model is implemented as external code, which is run independently from Apros. The simulations running within Apros require much greater time resolution than what is practical with the ray traced collector model, so interpolation

is used when computing values at each time instance. Depending on the number of computed ray tracing time steps, the user can choose between linear and polynomial interpolation. Linear interpolation is the simplest option and does not require additional user effort, but the results may be inaccurate between the interpolation points, as the path is not smoothed. Any residual noise resulting from the random sampling within the collector model is also preserved.

Simple well behaving and smooth interpolation over arbitrarily shaped data can be produced using Bernstein polynomials. By fitting a sufficiently high degree polynomial over the data, locally smooth interpolation can be achieved without affecting larger features. A Bernstein basis polynomial is defined by equation (48) (Timmerman, 2014, 2).

$$b_{i,n}(t) = \binom{n}{i} t^i (1-t)^{n-i} \tag{48}$$

Where n is polynomial degree,

i is an integer $0,\dots,n$ defining the index of the basis polynomial and

t is a scalar value $0..1$ where the function is evaluated

Any number of the Bernstein basis polynomials can be summed to produce a polynomial of the desired degree by equation (49).

$$B_n(t) = \sum_{i=0}^{n} \beta_i \, b_{i,n}(t) \tag{49}$$

where β_i are the Bernstein coefficient that define the shape of the curve. These coefficients are found by least squares fit over the ray trace data. The polynomial is first represented in matrix form, and the control points are solved by equation (50)

$$\boldsymbol{\beta} = (B^T B)^{-1} B^T \boldsymbol{y} \tag{50}$$

where B is a matrix where each basis polynomial has been evaluated for each normalized ray tracing time value, vector $\boldsymbol{y}$ contains the ray trace results corresponding to each time instance and vector $\boldsymbol{\beta}$ contains the Bernstein coefficients.

As the polynomial is only defined for the interval 0..1 the input data needs to be normalized within desired boundaries. In a more general case, even multidimensional relations can be modeled with generalization of Bernstein polynomials, the Bézier curves, surfaces and volumes, which are produced by linear combinations of multiple Bernstein polynomials. For the case at hand, this is not necessary, but it is useful to accumulate pragmatic and well behaving tools for future engineering applications.

This polynomial interpolation is implemented as the solar collector component in Apros, and it only takes day and time as inputs. The time value is given as hours since midnight as decimal value and the day is the number of days since start of the year. Day 1 is the 1st of January. At the beginning of each simulation run, the component invokes the external ray tracing utility. If the model parameters have been changed, the utility then performs the given ray tracing case, and returns tabulated results. The component then fits the polynomial over the result data and creates a fast lookup cache that can be read during the simulation with practically no computational cost. If the model parameters were not changed since the previous run, old lookup table is reused.

Apros has the ability to hide complex operations within a single diagram component. There are two distinct ways to do this: user components and external automation. User components work in similar fashion to programming functions. Their primary use is to hide complex diagrams behind one component, which can be used repeatedly. An example of this can be seen in Figure 5.1, where the component labeled "Receiver" is implemented as user component, whose full diagram can be seen in Figure 5.2. User components differ from regular functions in that the direction of data flow is not necessarily defined. Most sockets can act as inputs or outputs or both depending on operating conditions. Usually this means that the sockets define an input state, and output state is updated by the computation. User components are implemented directly within Apros using any number of other existing components.

External automation components work similarly to functions in most programming languages. Data is passed in through connections, computations are made based on data, and results are returned. The returned values are stored in the output sockets of

the component, where they are accessible to other Apros components. Implementation of external automation is done as external dynamic link library (dll), which is usually programmed with C, C++ or Fortran.
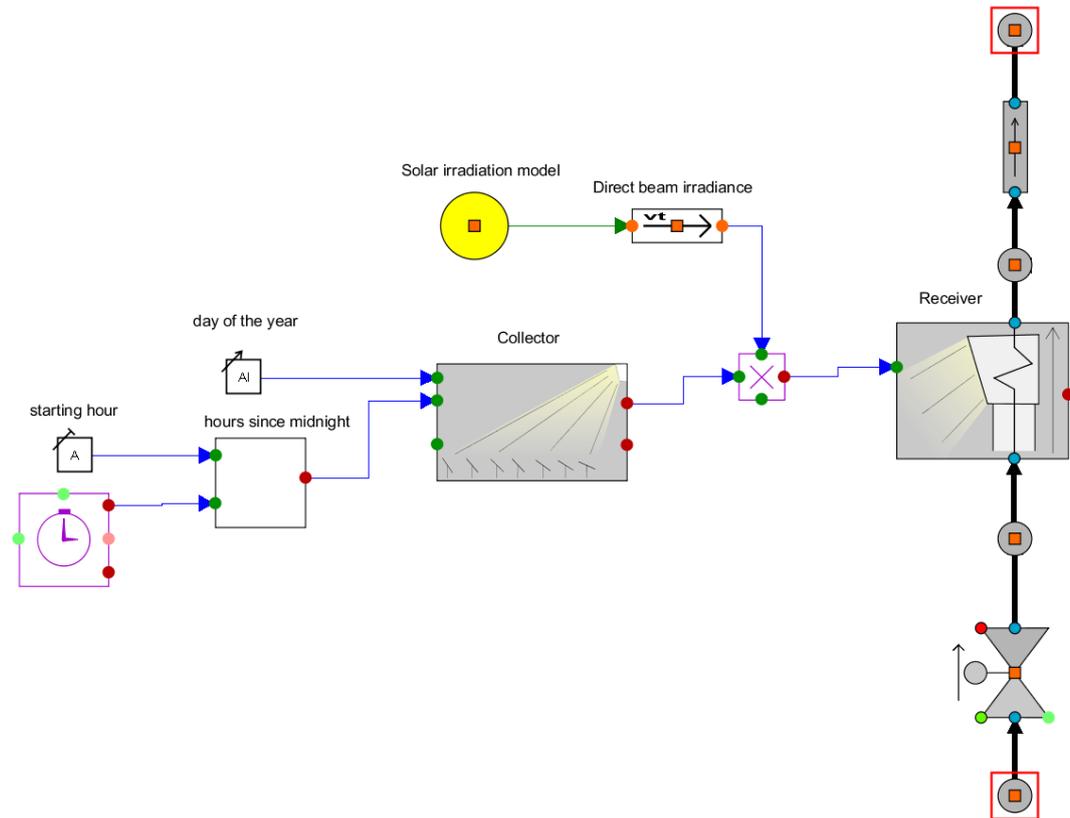

Figure 5.1: The central receiver system test configuration. The components labeled Collector and Receiver contain the presented model implementations. Collector acts as a wrapper for external computation. Receiver component contains another Apros model diagram seen in Figure 5.2

The collector component seen in Figure 5.1 acts as a wrapper for an external automation function, which does the interpolation discussed previously. It takes time information as inputs and outputs a scalar value for effective collector area in square meters. Apros module for solar radiation estimation outputs direct beam irradiance in units W/m^2 so the actual radiation power falling on the receiver is calculated by multiplying these two values. This value is then passed on to the receiver model component.

Since Apros can consider the incoming radiation as simple numerical data, in most cases the heat exchanger is represented by a pipe with a heating element. In Apros such component is called "heat pipe". In Figure 5.2 this component is labeled "Heat exchanger". The heating power of the heating element is continuously set to match the net irradiance at the solar tower receiver surface. This is done by passing power density value to the outer surface computation node of the heat pipe, which is represented by a cyan square labeled "Outer surface" in Figure 5.2. The appropriate power density is calculated by determining the effective heat transfer surface area on the heat pipe.
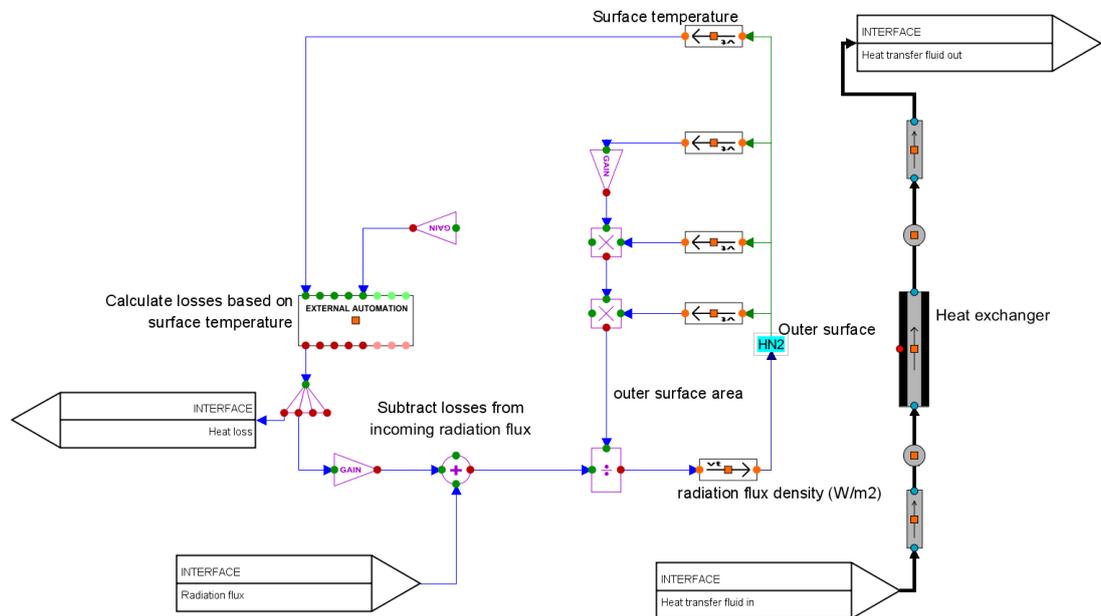

Figure 5.2: The receiver user component. Inputs and outputs are marked by white arrow flags, which correspond to the sockets of the receiver component seen in Figure 5.1

The computation node is also used to read the heat pipe surface temperature. The receiver heat loss model depends on surface temperature, while the surface temperature depends on the incoming net radiation and the properties and mass flow of the heat transfer fluid. Since the incoming net radiation in turn depends on the heat loss, this results in an iterative computation that quickly converges to the correct values within few simulation steps. The heat pipe surface temperature and the state

properties of the output heat transfer fluid are fully calculated by Apros computation nodes, and do not need any attention from implementation stand point.

Although the radiation flux is computed on a flat surface, the heat transfer surface is a pipe membrane wall with an area larger than that of a plane. The heat transfer surface area is calculated based on the pipe dimension and number of pipes. Only half the pipe wall is exposed to direct radiation, so only half of the pipe surface area is included in the calculation. This is illustrated in Figure 5.3. The radiation is assumed to spread evenly on the surface.
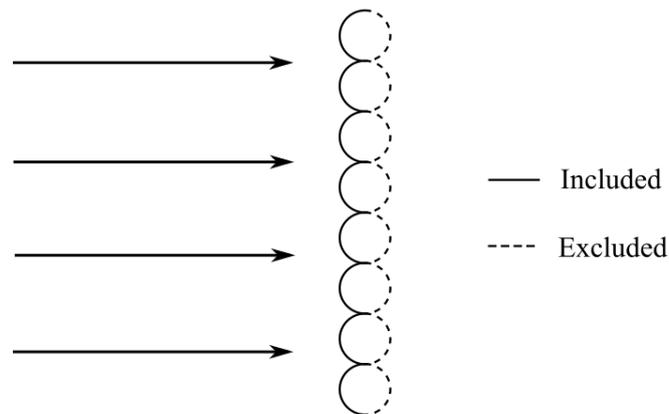

Figure 5.3: Radiation arriving at receiver heat transfer membrane wall. Solid line indicates area that is included in heat transfer calculations, and dashed line indicates area that is not included.

The heat exchanger used in the model acts as a boiler and a superheater in a once-through manner. Saturated water enters the heat exchanger at the bottom, and exists as superheated steam at the top. The surface temperature is assumed to be uniform across the entire receiver. This is not physically accurate configuration, but it is sufficient for verifying all the computations behind the model.

In a real model multiple heat exchangers and careful distribution of input heat can be utilized to more accurately model heat transfer characteristics and fluid dynamics of the receiver. More accurate modeling will also reveal any problem areas that improper fluid flow and elevated temperatures may cause. Conduction losses can be

also modelled by linking additional heat conduction components to the heat exchangers in the Apros model diagram.

The implemented Apros components take very few parameters and inputs, so most of the model settings have to be set by other means. An external configuration interface (Figure 5.4) is used to set up the simulation. The interface contains most of the parameters needed for simulation, but some must be imported as text files. Water vapor concentration and visibility data can be set as constant values, or time series data can be imported when desired. Most of the parameters are self-explanatory, and the built in context help provides information about all parameters.
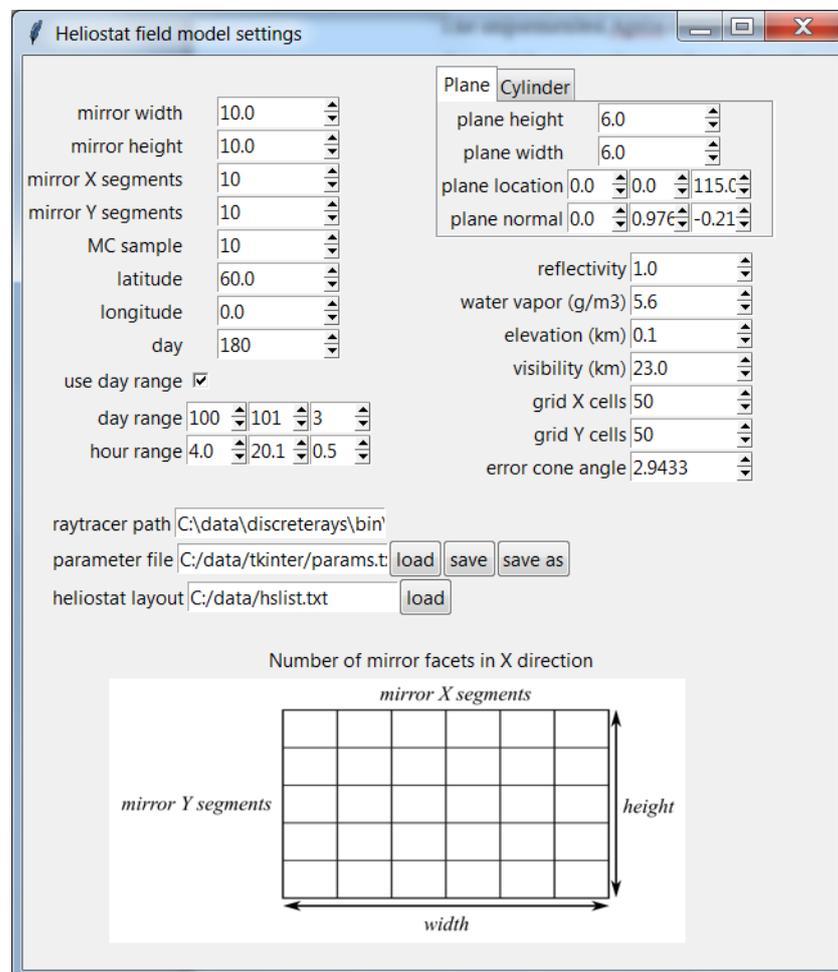

Figure 5.4: The external configuration interface.

The field layout is supplied as a text file, where each row contains 3 scalar values separated by space, representing the location coordinates (*x,y,z*) of each heliostat. How the field layout is generated is left to the user. In the following example cases, simple Python script is used to generate the field and Blender, a free software 3D modelling program, is used to model the field's physical boundaries and terrain topography. A simple method for generating field layout is presented in Appendix 2. The example does not aim to present the most optimal heliostat field configuration.

The location coordinate system is arranged the following way:

x : east	*y* : north	*z* : up
-*x* : west	-*y* : south	-*z* : down

At the beginning of each simulation run, Apros process executes the heliostat compute utility, if model parameters have been changed. If the settings are the same as in previous run, the old look-up table is reused.

5.2 Verification

To test the numerical accuracy and correct setup of the heat pipe acting as a heat exchanger, a simple energy balance test was done. The example does not aim to model a physical case, but rather is only intended to be used to verify that the absorbed heat flux returned by the receiver loss model is correctly added to the heat transfer fluid flow modeled by native Apros components.

Simple energy balance (51) was calculated with four different feedwater mass flows. Specific enthalpies were read from the two point nodes preceding and following the receiver model as seen in Figure 5.1. Calculations were done at 147 bar pressure and at saturation temperature of feed water 340,5 °C. Incoming solar flux from the collector was 80 MW in all cases.

$$\Phi_{\text{calc}} = \dot{m}_{\text{steam}} \cdot (h_{\text{out}} - h_{\text{in}}) \tag{51}$$

The calculated heat flux Φ_{calc} is compared to the incoming net radiation flux Φ_{in} absorbed by the receiver. All receiver losses have been accounted for in Φ_{in}, so the two flux values should match exactly. The comparison results shown in Table 5.1

are in good agreement. The right amount of heat is transferred to the steam loop. Remaining error is likely due to numerical errors and minor numerical diffusion from the heat pipe to the input node, which was not accounted for in the test. It can be seen that absorbed heat flux increases as heat transfer fluid mass flow increases. This happens because receiver heat losses decrease as receiver surface temperature decreases.

Table 5.1: Comparison of energy balance

$\dot{m}_{steam}$ (kg/s)	$T_{steam,out}$ (°C)	h_{in} (kJ/kg)	h_{out} (kJ/kg)	Φ_{in} (MW)	Φ_{calc} (MW)	difference (%)
27,2	820,3	1609	3993	64,9	64,7	0,26
34,5	658,1	1609	3623	69,7	69,5	0,32
42,1	545,6	1609	3331	72,8	72,4	0,52
45,1	509,7	1609	3229	73,6	73,1	0,64

6. DISCUSSION AND CONCLUSIONS

The physical principles governing central receiver systems are outlined in chapter 2 to produce suitably comprehensive view of the requirements set for the modelling task. Existing tools suitable for central receiver systems are explored in chapter 3, but as none of these were found adequate for long term use for projected use cases, a full model was developed specifically for use with Apros in dynamic simulations. Details for efficient implementation of the model are presented in chapter 4.

The ray tracing model was chosen because of the speed and adaptability it offers. The current implementation only covers a subset of all possible use cases and can be augmented with relative ease in the future. Compared to full ray tracing the number of necessary ray intersections was reduced by several orders of magnitude, which translates to considerable speed gains in computing. Multiple different factors affect the final computation time, and available development time did not allow building a clear and representative benchmark case for the speed gains. The presented grid-based ray tracing optimization is only two dimensional in its present implementation, and allows for efficient modeling of plants that have mirrors laid on reasonably flat terrain. This is largely not an issue since the majority of heliostat fields are arranged this way. Fields with uneven terrain (e.g. shallow slope or steeper hillside) can still be modeled, but performance may be somewhat lower due to higher exit conditions for rays.

A power distribution on the receiver surface can be efficiently computed with the presented Monte Carlo approximation of the error cone intersection, but some additional work is still needed to make the distribution information usable with Apros simulations. Although the total power may be computed accurately, the lack of distribution information may become a problem at later time as the Apros use cases become more complex and demanding. At the planning stages of the thesis work this was not considered major defect as the primary interest is the total average heat flux entering the heat transfer loop at any given time. However, this approach can give somewhat simplistic view of the receiver performance, and should be used with due care.

Furthermore, the heliostat aiming always uses the closest midpoint as target, and does not allow for different aiming strategies, which can lead to hotspots on the receiver. In a real receiver this could cause structural damage. In principle aiming is simple to implement, but the most efficient heuristics and control have not been considered sufficiently.

More comprehensive receiver model should be constructed for real world use cases. Such model would include different surface regions, where the radiation power would be distributed according to a distribution map build by improved collector model. Receiver losses would be calculated piecewise on all the individual regions. This would allow monitoring temperatures locally in each region as well as heat transfer fluid behavior such as local salt freezing within the receiver pipes.

The receiver model based on CFD simulations is designed for temperature averaged conditions, and its suitability for highly piecewise modeling needs to be determined. In the current implementation, the model can be used for planar, cylindrical, cavity and cubic (piecewise) receiver geometries with averaged surface temperature.

Receiver reflection loss was not directly considered in the model implementation, but for most cases it can be added as simple multiplier for the collector model output. In the receiver validation case in chapter 4.5.2, reflection loss was assumed to be 5%. More accurate models could be constructed experimentally by studying the reflection characteristics of receiver surface material at varying incidence angles and temperatures.

Sufficiently comprehensive full system validation data set was not found in literature, so validation of all model components were done individually. Results shown in chapter 4.5 show very good agreement for all comparison cases, and assuming correct implementation of communication between the models, the full model can be considered accurate. More validation work still needs to be done to establish full confidence in the model as a whole.

Ray tracing model validation was only performed with plane aperture receiver with a north field. Formal validation was not performed for cylinder receiver with a surrounding heliostat field. However, the ray tracing methodology is essentially the same for all primitive receivers and field layouts, so users can be reasonably confident in the model's correct operation even in these cases. Validation was also not done for the ESRA clear sky irradiance model as the implementation was not part of the thesis. The ray tracer implementation allows using measurement data for direct normal irradiation, which allows modeling of real world cases in real operating conditions. Measurement data should always be preferred over estimations, and therefore the clear sky model should only be used as a rough guideline before such data is available. For this reason validating the ESRA model was not considered a high priority task in the thesis.

7. SUMMARY

The thesis work was conducted as a part of master's thesis studies in Lappeenranta University of Technology and it was commissioned by VTT Technical Research Centre of Finland Ltd. The work was done in the time period of 8 months from September 2015 to April 2016. Solar power is fairly new field of study for VTT, but considerable amount of work has been done over the past several years to enhance solar power modelling capabilities of Apros, and to acquire world class expertise in the field. While concentrated solar power is not economical in Finland, interest exists around the world for design and modelling of new solar power plants, and the dynamic modelling capabilities of Apros provide excellent simulation platform for any solar thermal plant. This thesis work was conducted to augment the Apros tool pipeline with central receiver modeling capabilities. The developed model had to be made fast and accurate in order to function efficiently within dynamic process simulation environment.

The preliminary work included a study for the physical principles involved in concentrated solar power. Several distinct phenomena were identified, which could be implemented as separate interconnected models: the collector optical behavior, the receiver heat loss and heat transfer model, local radiation attenuation and global atmospheric loss. Literature of the field was then surveyed for suitable correlations and computational models, which would most accurately represent the physical phenomena, while remaining sufficiently fast for dynamic simulation.

Survey on existing central receiver modelling tools revealed that most methods fall on two extremes; the physically accurate ray tracers and fast analytical approximations. Ray tracing tools have excellent accuracy, but require considerable amount of processing time. Analytical approximations are very fast, but are limited in scope, and do not necessarily give physically accurate results in all conditions. The requirements of the presented model needed a solution that would fall between these two extremes.

The optical behavior of radiation was the most significant challenge of the development effort. A fast and accurate approximation method was found in

literature (Noone et al.,2012), and it was modified and adapted to suit the particular needs of this thesis work. The method uses a discrete ray tracing approximation, which works similarly to existing Monte Carlo ray tracing, but reduces the number of required ray intersections considerably. Each mirror surface is divided into smaller facets and only a single ray is traced for each. Such a ray has the radiation power proportional to the surface area of the facet. Each ray reflecting from a mirror is enveloped by an error cone, whose opening angle is proportional to the uncertainty of the ray's travel direction. This uncertainty is caused by mirror surface imperfections, sun's apparent shape in the sky and atmospheric imperfections. The radiation power falling on the central receiver is calculated by the intersection between the cone and the receiver surface. A simple random sampling approximation was implemented to make the model adaptable to all future use cases. The model was implemented as an external computation utility written in high performance C-code. The ray tracing results are cached to a file, and are used by Apros during power plant simulations.

A model by (Pitman & Vant-Hull, 1984) was chosen as the local radiation attenuation model. This model is more widely applicable than the model by (Vittitoe & Biggs, 1978), which is often used in the industry. The model results also match numerical atmospheric databases more closely (Ballestrín & Marzo, 2012). Global atmospheric loss model was not implemented as part of the thesis as an Apros component already exists for this purpose. Upon examination, the existing component was deemed sufficiently accurate. A model by Kim et al. (2015) was chosen as the central receiver heat loss model. It is a correlation model based on large number of CFD simulations. This model works across most receiver types, temperatures and wind conditions, making it ideally suited for experimentation with different setups in variety of conditions.

Construction of a full power plant model was not part of the thesis. Small section of a power plant steam loop was produced in Apros for testing the correctness of the heat exchanger process. Resulting radiation power from the receiver model is passed on to a heat exchanger which transfers the heating power to the Apros model. From this point forward, the process is fully simulated by existing Apros components.

Validation of the model was done for each model component separately, as sufficiently comprehensive validation data set was not found for complete validation. The ray tracing model was validated by a comparison study with equivalent Soltrace simulation. Results from the local atmospheric attenuation model and the receiver heat loss correlation model were compared against the data in their respective reference papers. In all cases the results were shown to be in good agreement with each reference case data. Energy balance examination was done to verify, that the right amount of power is entering and exiting the heat exchanger at any time. The energy balance was calculated at a number of heat transfer fluid mass flow values, and the results showed that the heat exchanger is working correctly. Although all model components are shown to work accurately and the full model appears to function correctly, full model validation against experimental data is still needed to establish full confidence in the model.

REFERENCES

Amanatides, John; Woo, Andrew. 2010. A Fast Voxel Traversal Algorithm for Ray Tracing. Dept. of Computer Science, University of Toronto.

Badescua, Viorel; Gueymard, Christian A.; Cheval, Sorin; Oprea, Cristian; Baciu, Madalina; Dumitrescu, Alexandru; Iacobescu, Flavius; Milos, Ioan; Rada, Costel. BadescuComputing global and diffuse solar hourly irradiation on clear sky. Review and testing of 54 models. Renewable and Sustainable Energy Reviews 16 (2012) 1636– 1656.

Ballestrín, Jesús; Marzo, Aitor. 2012. Solar radiation attenuation in solar tower plants. Solar Energy, Volume 86, Issue 1, January 2012, Pages 388–392

Buie, D.; Monger, A.G. 2004. The effect of circumsolar radiation on a solar concentrating system. Solar Energy 76 (2004) 181-185.

Cardemil, JM; Starke, AR; Scariot, VK; Grams, IL; Colle, S. 2014. Evaluation of solar radiation models to assess the effects of climate and geographical location on the heliostat field efficiency in Brazil. SolarPACES 2013. Energy Procedia 49 (2014) 1288-1297.

Dogniaux R. 1986. The estimation of atmospheric turbidity. In: Proc Advan European Solar Radiation Climatol London UK, UK Int Sol Energy Soc. p.3.1–4.

Duffie, John A.; Beckman, William A.. 2013. Solar Engineering of Thermal Processes (4th Edition). John Wiley & Sons. Print ISBN:9780470873663. eBook ISBN:9781118418123. OCLC Number:841584921

Google HOpS documentation. (no date).[Web page] Heliostat optical simulation software source code. Available in: https://github.com/google/hops

Gueymard, Christian A.. 2003. Direct solar transmittance and irradiance predictions with broadband models. Part I: detailed theoretical performance assessment. Solar Energy 74 (2003) 355–379.

IEA. 2014. Technology Roadmap; Solar Thermal Electricity; 2014 edition. International Energy Agency.

IEA. 2015. Tracking Clean Energy Progress 2015; Energy Technology Perspective 2015 Excerpt; IEA Input to the Clean Energy Ministerial. International Energy Agency.

Kaskaoutis, D. G.;Kambezidis, H. D.;Hatzianastassiou, N.;Kosmopoulos, P. G.;Badarinath, K. V. S..2007. Aerosol climatology: dependence of the Angstrom exponent on wavelength over four AERONET sites. Atmos. Chem. Phys. Discuss., 7, 7347–7397, 2007

Kim, Jongkyu; Kim, Jin-Soo; Stein,Wesley; 2015. Simplified heat loss model for central tower solar receiver. Solar Energy 116. Pages 314-332.

Lee, Hyunjin. 2014. The geometric-optics relation between surface slope error and reflected ray error in solar concentrators. Solar Energy 101 (2014) 299-307. Solar Energy Department, Korea Institute of Energy Research.

Müller-Steinhagen H. 2013. Concentrating solar thermal power. Phil Trans R Soc A 371: 20110433.

Noone, Corey J.; Torrilhon, Manuel; Mitsos, Alexander. 2012. Heliostat field optimization: A new computationally efficient model and biomimetic layout. Solar Energy 86, pages 792–803

Pacheco, E.. 2002. Final test and evaluation results from the solar two project. SAND2002-0120.

Page, J.K.. Prediction of Solar Radiation on Inclided Surfaces. Solar Energy R&D in the European Community. Series F, Volume 3. Solar Radiation Data. D.Reidel Publishing Company. ISBN 90-277-2260-9.

Pitman CL; Vant-Hull LL. 1984. Atmospheric transmittance model for a solar beam propagating between a heliostat and a receiver. Sandia National Laboratories,.SAND83-8177.

Richter, Christoph; Gueymard, Christian, A; Lincot, Daniel. 2013. Solar Energy. Springer New York Dordrecht Heidelberg London. Springer Science+Business Media. ISBN 978-1-4614-5806-7.

Romero-Alvarez, Manuel; Zarza, Eduardo. 2007. Handbook of Energy Efficiency and Renewable Energy, chapter 21. CRC press. Taylor & Francis Group, LLC.

Sandia National Laboratories. [web page] National solar thermal test facility. [cited 19.4.2016] Available in: http://energy.sandia.gov/energy/renewable-energy/solar-energy/csp-2/nsttf/

Schell, Steve. 2011. Design and evaluation of esolar's heliostat fields. Solar Energy 85 (2011) 614-619.

Schramek, Philipp; Mills, David R. 2003. Multi-tower solar array. Solar Energy Volume 75, Issue 3, September 2003, Pages 249–260

Solar Reserve (no date). [web page] Crescent dunes. [cited 20.4.2016]. Available in:

http://www.solarreserve.com/en/global-projects/csp/crescent-dunes

Soltrace website. (no date). [web page] Optical ray tracing software. [cited 10.5.2016] Available in: http://www.nrel.gov/csp/soltrace.html

Taylor, Alan. 2014. [web page] The Ivanpah Solar Electric Generating System. [cited 26.4.2016]. The Atlantic. Available in:
http://www.theatlantic.com/photo/2014/03/the-ivanpah-solar-electric-generating-system/100692/

Timmerman, Grant. 2014. Approximating Continuous Functions and Curves using Bernstein Polynomials. University of Washington.

Tonatiuh website. (no date). [web page] Optical ray tracing software. [cited 15.3.2016] Available in: https://github.com/iat-cener/tonatiuh

Vittitoe, C. N.; Biggs, F. 1978. Terrestrial Propagation LOSS. Presented Amer. Sec. ISES meeting, Denver, August 1978. Sandia release SAND78-1137C.

Wendelin, T. (2003). SolTRACE: A New Optical Modeling Tool for Concentrating Solar Optics. Proceedings of the ISEC 2003: International Solar Energy Conference, 15-18 March 2003, Kohala Coast, Hawaii. New York: American Society of Mechanical Engineers, pp. 253-260; NREL Report No. CP-550-32866.

Appendix 1 Calculating sun direction vector

A method for calculating solar direction is described in (Duffie & Beckman, 2013, chapter 1, p13). This model returns solar azimuth and elevation angles based on time and day of the year. Additionally a solar direction vector is calculated based on the angles. As seen in Figure A 1, solar elevation angle is defined as the angle between horizontal plane and solar direction. Azimuth is defined as the angle between south direction and the sun direction's 2-dimensional projection on the horizontal plane. Positive azimuth direction is clockwise.
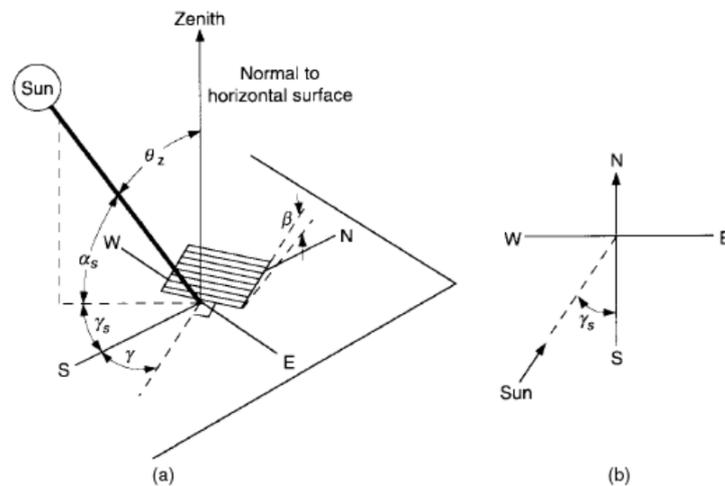

Figure A 1: Definitions of solar angles (Duffie & Beckman, 2013, chapter 1, p13)

Initially the solar declination is calculated based on day of the year.

$$\delta = \frac{\pi}{180} 23{,}45 \sin\left(2\pi \frac{284 + n}{365} \right)$$
(A-1)

Where δ is solar declination angle in radians and

$\quad\quad n$ is the day number

The hour angle is defined by equation (A-2). The angle is negative before noon and positive after noon. This equation is based on the fact that the earth rotates 15 degrees in one hour.

$$\omega = \frac{15}{180}\pi\,(t - 12) \tag{A-2}$$

Where ω is the hour angle in radians

t is the hours since midnight

Based on the declination and hour angle, the solar zenith angles is calculated by equation (A-3)

$$\theta_z = \cos^{-1}(\cos\phi\cos\delta\cos\omega + \sin\phi\sin\delta) \tag{A-3}$$

Where θ_z is solar zenith angle in radians and

ϕ is latitude

Solar azimuth angle γ_s is now calculated by (A-4).

$$\gamma_s = \text{sign}(\omega)\left|\cos^{-1}\left(\frac{\cos\theta_z\sin\phi - \sin\delta}{\sin\theta_z\cos\phi}\right)\right| \tag{A-4}$$

The sign function returns 1 if the argument is positive and -1 otherwise. Elevation angle is defined by the zenith angle using equation (A-5).

$$\alpha_s = \frac{\pi}{2} - \theta_z \tag{A-5}$$

To use the correct coordinate system for sun vector calculations, the azimuth angle is redefined as starting from positive east direction with counterclockwise positive direction.

$$\gamma_c = -\frac{\pi}{2} - \gamma_s \tag{A-6}$$

The x, y and z components of the unnormalized solar heading $\boldsymbol{n}_{0,\text{sol}}$ can be derived from simple trigonometric functions based on the geometry.

$$\boldsymbol{n}_{0,\text{sol},x} = \cos\gamma_c \tag{A-7}$$

$$\boldsymbol{n}_{0,\text{sol},y} = \sin\gamma_c$$

$$\boldsymbol{n}_{0,\text{sol},z} = \tan\alpha_s$$

Finally the equivalent unit vector for solar heading is obtained by normalizing the heading vector to its magnitude.

$$\boldsymbol{n}_{\text{sol}} = \frac{\boldsymbol{n}_{0,\text{sol}}}{|\boldsymbol{n}_{0,\text{sol}}|} \tag{A-8}$$

Appendix 2 Heliostat field geometry generation

A simple method for generating field layouts is described in (Noone et al., 2012). This method generates a phyllotaxis pattern based on sampling discrete locations on Fermat's spiral. The points are first defined in polar coordinates. Polar angle of the point is given by equation (A-9).

$$\theta = n \cdot \frac{2\pi}{\varphi^2} \tag{A-9}$$

where n is the index of the generated point and

$\varphi = \frac{1+\sqrt{5}}{2}$ is the golden ratio.

Radial coordinate r, i.e. the distance from origin, for the point n is defined by equation (A-10).

$$r = a \cdot n^b \tag{A-10}$$

where a and b are some suitably selected constants that influence the shape of the pattern. Cartesian x and y coordinates can then be calculated by equations (A-11) and (A-12).

$$x = r \cos \theta \tag{A-11}$$

$$y = r \sin \theta \tag{A-12}$$

Large number of points is generated and the optimal locations are selected based on desired criteria, such as highest overall mirror efficiency, physical boundaries and other physical constraints. Generated example layout is seen in Figure A 2.
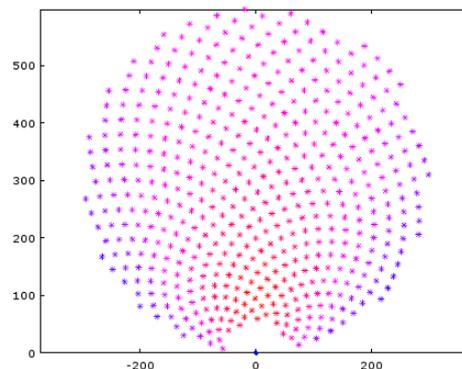

Figure A 2: Heliostat field layout generated by the phyllotaxis method